

CHALMERS TEKNISKA HÖGSKOLA
Institutionen för Termo- och Fluidodynamik



CHALMERS UNIVERSITY OF TECHNOLOGY
Department of Thermo and Fluid Dynamics

Paper 2

A Numerical Study of Unsteady Two-Dimensional Flow Around Rectangular Cylinders at Incidence

By

Sohankar, A., Norberg, C. and Davidson, L.

Internal Report Nr. 96/25, Department of Thermo and Fluid Dynamics,
Chalmers University of Technology, Gothenburg, Sweden

Göteborg, May 1996

A Numerical Study of Unsteady Two-Dimensional Flow Around Rectangular Cylinders at Incidence

Ahmad Sohankar¹, Christoffer Norberg² and Lars Davidson¹

¹Thermo and Fluid Dynamics
Chalmers University of Technology
412 96 Göteborg, Sweden

²Division of Heat Transfer
Lund Institute of Technology
221 00 Lund, Sweden

Abstract

Calculations of unsteady 2D-flow around rectangular cylinders at incidence are presented. The Reynolds numbers are low so that the flow presumably is laminar. Experimental results, at these low Reynolds numbers, are rather scarce. When available, however, the global flow periodicity and the mean drag, respectively, seems to be well predicted. An incompressible SIMPLEC code is used employing non-staggered grid arrangement. A third-order QUICK scheme is used for the convective terms. The time discretization is implicit and a second-order Crank-Nicolson scheme is employed. The sensitivity of calculation domain sizes upstream, downstream and sideways (solid blockage) as well time and spatial resolution, respectively, is investigated. The influence of cylinder side ratio ($B/A = 1, 2, 4$) at various angles of incidences ($\alpha = 0^\circ - 90^\circ$) and for $Re = 100, 200$ is investigated. A number of quantities such as Strouhal number, lift and drag coefficients and various surface pressure coefficients are calculated.

1 Introduction

From the days of Leonardo da Vinci or maybe earlier, the flow around slender cylindrical bluff bodies has been a source of fascination and intricacy and thus this flow situation has stimulated and attracted a waste amount of research studies. However, it was not until 1878, when Strouhal published his pioneering paper [60] on singing wires due to vortex shedding, that this type of flow turned into a subject of quantitative research. The flow situation is popular not only because of its academic attractiveness but also due to its related technical problems associated with energy conservation and structural design. For instance, fuel-consumption of aircrafts and road vehicles might be decreased by reducing aerodynamic drag and multi-storey buildings such as skyscrapers ought to be designed so as to minimize convective heat loss and dust deposits. In addition, structures must be designed so as to avoid potentially disastrous wind-induced oscillations and knowledge of vortex shedding characteristics is crucial in the design of vortex shedding flowmeters.

Slender bluff body cross flow configurations arise in numerous industrial applications and environmental situations, e.g. flow-metering devices; cooling of electronic components and equipment; the obstructed spaces between co-rotating disks in magnetic disk storage devices; tall buildings and other technical structures such as cooling towers, chimneys, off-shore platforms, pipelines, periscopes, tubular heat exchangers, suspension bridges, towers, pylons, poles, cables,

masts and wires. Bluff-body induced-flow unsteadiness and mixing may also be used to enhance heat and mass transfer to or from the bluff body and/or its surroundings.

Aside from the above practical motivating factors, the unsteady flow and heat transfer associated with cylindrically shaped bluff bodies are interesting in their own right and have been the subject of considerable basic research. In these studies the principal objective has mostly been to measure and/or calculate the field variables and related quantities from which to determine cylinder drag and lift coefficients as well as Strouhal and Nusselt numbers. The studies can be classified according to the number, arrangement and cross-sectional shapes of the cylinders, the character of the approaching flow and whether it is of a free-stream or confined type.

A bluff body is one in which the flow under normal circumstances separates from a large section of body surface thus creating a massive wake region downstream. We now consider a slender bluff body of constant cross sectional area, i.e. a cylinder, exposed to a cross flow with a constant free stream velocity, U_∞ . An appropriate Reynolds number is then $Re = U_\infty d/\nu$, where d is the projected width of the cylinder in the streamwise direction. As a rule of thumb, significant separation then occurs at Reynolds numbers above unity. In this flow situation there are two free shear layers that trail aft in the flow bounding the wake region. Since the innermost portion of the free shear layers moves much more slowly than the outermost portion of the layers which are in contact with free stream, the free shear layers tend to roll up into discrete, swirling vortices. At a sufficiently high Reynolds number and due to wake instability mechanisms, the vortical region downstream of the body emanates into the phenomenon of vortex shedding characterized by an unsteady periodic flow situation in which the separated vortices are “shed” alternately from the upper and lower side of the body. A non-dimensional shedding frequency is called the Strouhal number, in this context defined as $St = f_S d/U_\infty$. The near-wake flow unsteadiness gives rise to fluctuating drag and lift forces which can stress the body by making it vibrate. Cylinder vibration can, among other things, (i) increase the vortex strength, (ii) increase the spanwise wake correlation and (iii) force the shedding frequency to match the vibration frequency (lock-in or synchronization)[6]. In addition, the associated fluctuating pressures is a source of acoustical emission.

The first mathematical treatment of of vortex shedding was, in 1911, given by von Kármán in [22] and the staggered vortex configuration (in a moving frame of reference) is usually referred to as the von Kármán vortex street. Vortex streets are formed in the wakes of bluff bodies over a wide range of Reynolds numbers, from approximately 50 to 10^6 and even higher [19]. In an ideal free stream flow situation, vortex shedding commences at some specific critical Reynolds number, Re_c , which is solely dependent on the cross section geometry and flow incidence. For instance, for the circular cylinder in cross flow [35], where flow incidence is irrelevant, Re_c is about 47. For the square cylinder at zero incidence, i.e. with one side surface facing the oncoming flow, the investigations of Kelkar & Patankar [23] and Sohankar *et al.* [59] indicate that Re_c is between 50 and 55. Critical values in other cylinder flow situations can be found in Jackson [21]. Quite recently, the commencement of the vortex shedding process has successfully been described as a self-excited limit-cycle oscillation of the wake, in which the critical onset value is reached through a supercritical Hopf bifurcation of the steady wake [52]. Recent advances in stability theory and related experiments have shown that the vortex shedding formation is a result of a global absolute instability [31, 57] in which the characteristics of the flow at Reynolds number close to but higher than Re_c can be described by a single Stuart-Landau equation. Although significant progress has recently been achieved, see e.g. Williamson [69] for a review, a complete description of the shedding process at higher Re is still lacking. Nevertheless, by increasing the Reynolds number from the onset value it is indicated that there are associated increases in non-dimensional vortex strength (suitably defined), Strouhal number and fluctuating force

coefficients [56]. In the laminar régime, which usually persists up to Reynolds numbers of about 200, the vortex shedding is characterized by a very well-defined frequency. As Re increases still higher, the vortices become less and less “regular”; in other words, for successively higher Reynolds numbers, the effects of flow three-dimensionality and turbulence become more and more pronounced.

2 Motivation

From an engineering point of view and for several reasons, it is necessary to extensively study flow-induced vibration from sharp-edged rectangular cross-sectional cylinders. First, with the use of high-strength materials, structures are more slender and more susceptible to vibration. The development of modern materials and construction techniques has resulted in the emergence of a new generation of structures that are often, remarkably flexible, low in damping, and light in weight. Such structures generally exhibit an increased susceptibility to the action of fluid flow. Accordingly, it has become necessary to develop tools enabling the designer to estimate flow-induced effects with a higher degree of refinement than was previously required. It is the task of the engineer to ensure that the performance of structures subjected to the action of fluid flow will be adequate during their anticipated life from the standpoint of both structural safety and serviceability. To achieve this end, the designer needs information regarding (1) the flow environment, (2) the relation between that environment and the forces it induces on the structure, and (3) the behavior of the structure under the action of these forces [12]. Second, in many cases, high-velocity fluid flowing through the components of devices is required, e.g. in advanced nuclear power reactors, and this may cause detrimental vibrations. Third, the dynamic interaction between the structure and the fluid is one of the most fascinating problems in engineering mechanics. The prediction of amplitudes and dominating frequencies related to flow-induced sound and vibration is of great importance in structural design. In addition, the study of bluff-body wakes and its associated fluid forces and wake frequencies can be motivated from a purely fundamental basis. Fourth, regardless of the disadvantages of sharp-edged rectangular cross-sectional shapes, particularly their susceptibility to flow-induced vibration, frequently these non-ideal rectangular geometries are employed in the design of structures. This is because the fluid dynamic considerations are often only one aspect of the design process and may play a subsidiary role to other aspects such as economics, ease of construction or structural requirements. Structures that typically have rectangular or near-rectangular cross section, include architectural features on buildings, the buildings themselves, beams, fences and occasionally stays and supports in internal flow geometries.

Further, situations may arise in which the designer need to choose the rectangular cross-sectional member with incidence relative to the mean flow direction. In such cases, knowledge of the mean and fluctuating flow-induced loading as well as expected near wake frequencies is useful e.g. in determining whether the structure may experience vortex-induced vibrations [6]. In addition, a structure vibrating in a plunging mode experiences a time-dependent effective change in the angle of incidence and the associated changes in forces and moments might initiate the instability phenomenon usually referred to as galloping, see e.g. [37, 48]. If the vibrations are severe enough especially when the oncoming flow is at an angle of attack relative to the body, they may lead to structural failure. Thus, investigations on the effect of incidence are strongly motivated.

In addition, of interest to engineers are not only the integral parameters such as Strouhal number, drag and lift coefficient but also the local dynamic loading of a bluff body placed in a fluid stream.

Except perhaps for the circular cross section, detailed knowledge on the unsteady flow field

around cylinders is rather limited owing to the considerable effort involved in taking unsteady measurements and calculations in such flows. Consequently, there is a considerable gap of knowledge concerning the effects of flow incidence at various Reynolds number and for different cross section geometries. For rectangular cylinders in cross flow and by means of numerical simulation, one objective of the present research is to partially fill out this gap. Another objective is aimed towards a better understanding of the vortex shedding phenomenon.

3 Problem Under Consideration

The problem under consideration is depicted in Fig. 3. A fixed two-dimensional rectangular cylinder with a side ratio B/A , where B is the longest side of the cylinder, is exposed, at some angle of incidence α , to a constant free stream velocity U_∞ . Incompressible viscous flow with constant fluid properties is assumed. Unless otherwise stated, all dimensions are scaled with the projected width of the cylinder in the streamwise direction, $d = A \cos \alpha + B \sin \alpha$ ($0^\circ \leq \alpha \leq 90^\circ$). The scaling with d also applies to Reynolds and Strouhal numbers. The vertical distance between upper and lower walls, H , defines the solid blockage of the confined flow (blockage parameter $\beta = d/H$). Velocities are scaled with U_∞ and physical times with d/U_∞ . Forces and moments acting on the cylinder are scaled with d and the dynamic pressure of the upstream flow $\rho U_\infty^2/2$. Pressure coefficients are defined as $C_p = 2(p - p_\infty)/\rho U_\infty^2$, where p_∞ is the static pressure of the upstream flow. Calculated pitching moments are referred to the geometrical center with positive values in the anti-clockwise direction. Other quantities are defined in the nomenclature list.

4 Review

When considering vortex shedding flow around cylinders, a large amount of experimental and numerical studies have been carried out for the circular cross section, i.e. flow around circular cylinders. Cylinders at other cross sections have received much less attention. Nevertheless, in recent years, quite a number of investigations (mostly numerical) have considered rectangular cylinders in cross flow. However, except perhaps for the experimental studies on the square section, the effects of flow incidence have not been extensively covered.

In the following a short review on significant numerical and experimental results on flow around sharp-edged cylinders is given.

4.1 Experimental

At high Reynolds numbers, a large number of experimental investigations on the flow around rectangular cylinders have been performed, see [24] for a review. However, there are only a few such investigations at low to moderate Re , i.e. $Re < 10^3$. The rectangular cylinder in cross flow did not become prevalent until the mid 1960:s and early 1970:s [67, 33, 4]

A large amount of experimental data has been gathered at angles of incidence $\alpha = 0^\circ$ and/or $\alpha = 90^\circ$, i.e. with one side of cylinder facing the flow. In such investigations the results usually are presented with h/d as a parameter. Fig. 1 displays, at $Re > 10^3$, a compilation of Strouhal numbers and mean drag coefficients *vs.* h/d . As shown in Fig. 1b a maximum occurs at around $h/d = 0.6$, also see e.g. [33, 4, 35, 46, 9, 2]. Probably, this phenomenon is related to an interaction between the separated shear layers and the downstream part of the body, see e.g.

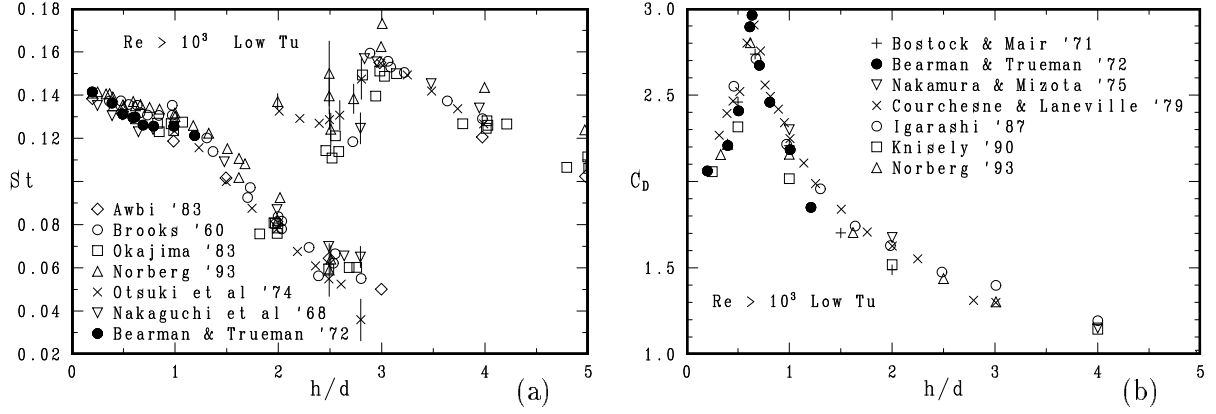


Figure 1: Strouhal number (a) and mean drag coefficient (b) vs. h/d .

[43, 39]. As shown in Fig. 1a, in turbulent flow there is also a jump behavior in the Strouhal number which occurs in between $h/d = 2$ and $h/d = 3$.

Mean and fluctuating pressure fields acting on a quadratic cylinder ($B/A=1$) in both uniform and turbulent flows, were in 1975 presented by Lee [25] ($Re = 1.8 \times 10^5$). He observed that when the cylinder was rotated with respect to the flow, the vortex formation region moved downstream causing the drag to decrease. A minimum value of the drag was reached at an angle of incidence of about 15° . Further rotation of the cylinder produced a gradual increase in the drag as the vortex formation region moved upstream after the flow had reattached to the side walls. He also observed that the Strouhal number increased to a maximum at the angle at which the mean drag was minimum.

Bearman & Trueman [4] considered rectangular cylinders with projected side ratios from $h/d = 0.2$ to 1.2 ($Re = 2 \times 10^4$ to $Re = 7 \times 10^4$). Detailed measurements on base pressures, mean drag and shedding frequency as well as flow visualizations were presented. The existence of a maximum in drag at an intermediate value in h/d , as previously found in 1968 by Nakaguchi et al. [33], was confirmed. At the critical side ratio $h/d = 0.62$ the maximum drag coefficient was found to be 2.94, see Fig. 1b.

One of the most extensive investigation was carried out by Okajima [40] (1982). He determined Strouhal number of rectangular cylinders at zero incidence with side ratio 1 to 4 in the range of Reynolds number between 70 to 2×10^4 . He found a certain range of Reynolds number for cylinders with side ratio 2 and 3 where flow pattern abruptly changes with a sudden discontinuity in Strouhal number. For Reynolds number below this region, the flow separated at the leading edges reattaches on either the upper or the lower surface during a period of vortex shedding while, for Reynolds number beyond it, the flow fully detaches itself from the cylinder.

Extending the experimental studies by Vickery (1966), Lee (1975), Okajima (1982) to lower values of the Reynolds, Hasan [20] (1989) conducted an experimental investigation of the flow past a fixed square cylinder at different angles of incidence in the range of Reynolds number from 6720 to 43000. He observed that the value of the Strouhal number, based on the projected width of the cylinder, increased upon increasing the angle of incidence, reached a maximum at 22.5° and then decreased with further increase in the angle of incidence. The maximum value of the Strouhal number was about 15% higher than those reported by Vickery and Lee. However, the trend of the Strouhal number was the same. Hasan explained this trend by the fact that the flow reattached at the leeward upper corner of the square cylinder at an angle of incidence of about 22.5° . This would reduce the wake width as compared to case when the flow did not

reattach. The reduced wake width would give rise to a closer longitudinal spacing of the shed vortices, which was equivalent to an increase in the frequency of vortex shedding. This would also explain the decrease of the Strouhal number value as the angle of incidence increased from 22.5° to 45° .

Knisely [24] (1990) has a more complete review on experimental results. He experimentally determine Strouhal numbers for a family of rectangular cylinders with side ratios ranging from .04 to 1 and with angles of attack 0° to 90° . Tests were conducted both in a water channel with Reynolds numbers between 7.2×10^2 and 3.1×10^4 and in a wind tunnel with Reynolds numbers between 8.8×10^3 and 8.1×10^4 , based on the projected cross stream dimension and mean velocity. He explain that the Strouhal number, except for the thinnest plate have qualitatively similar behavior with changing angle of attack. The general tendency is a rapid rise in the Strouhal number occurs at relatively small angles of attack. This rapid rise is associated with reattachment of the separated shear layer. The angle of attack where reattachment and, hence, the rapid rise in Strouhal number occurs is dependent on the side ratio. After the sudden rise, the Strouhal number levels off with a further increase in angle of attack. As the angle of attack approaches 90° , there is a sudden decline in the value of the Strouhal number, again associated with shear layer-corner interaction (i.e. detachment). For the thinnest plate, the Strouhal number was found to be essentially independent of the angle of attack over a wide range of angles.

Norberg [34] (1993) studied the flow around and pressure forces on fixed rectangular cylinders at angles of attack $0^\circ - 90^\circ$. Investigated body side ratios were $B/A = 1 - 5$ and Reynolds numbers ranged from about 400 to 3×10^4 (pressure measurements from about $Re = 3 \times 10^3$). Multiple wake frequencies were registered at low angles of incidence, within certain Reynolds number ranges, and at side ratios $B/A = 2 - 3$. The flow showed a large influence of both angle of attack and side ratio due to e.g reattachment and shear layer/edge interactions. Also some calculations of quasi-steady galloping response in the plunging mode for the square cylinder were presented.

Zaki *et al.* [70] (1994) studied flow around a fixed and freely rotatable square cylinder in the range of Reynolds number from 1000 to 10,000 and variation of shedding frequency with cylinder orientation for the fixed cylinder. They observed that the rotatable cylinder show four distinct regimes of motion: a stable position where the cylinder side surfaces are parallel to the flow, periodic oscillations about this position, rotation with reversal of direction, and autorotation.

Along the same line but for different afterbody shape of bluff bodies Luo *et al.* [28] (1994) investigated the effects of the afterbody shape and angle of incidence on the structure of the flow past a prismatic body. They used four cross-sectional shapes with identical upstream facing side, a square, two trapeziums, and a triangle, in wind tunnel and water tunnel. They concluded that the differences in the afterbody shape will affect the structure of the flow and, hence, both the magnitude and frequency of the aerodynamic loading on the prismatic body. Their experiments showed that no cross-sectional shape is absolutely stable to galloping oscillation because a shape that is a stable to galloping oscillation at a certain mean angle of incidence may become unstable at a different mean angle of incidence.

Further data on rectangular cross section cylinders can be found in papers by Nakaguchi *et al.* [33](1968), Parkinson [49] (1971), Bearman & Trueman [4] (1972), Bearman & Trueman [3] (1972), Novak [36] (1974), Novak [37] (1974), Rockwell [54] (1977), Otsuki *et al.* [45] (1978), Washizu *et al.* [68] (1978), Ohya *et al.* [39] (1980), Grant & Barnes [18] (1981), Okajima [40] (1982), Modi & Slater [30] (1983) Bokaian & Geoola [8, 7] (1982, 1983), Obasaju [38] (1983) and Parker & Welsh [47] (1983).

In all these studies the Reynolds numbers are relatively high, ranging from about $Re = 10^3$ to $Re = 10^5$. At Reynolds numbers relevant to this study, i.e. $Re \leq 250$, the only experimental results available in the open literature seems to be Okajima [40, 43], Davis & Moore [14] (1982) and Okajima [42] (1995).

4.2 Numerical

One of the most important problem which the earlier numerical researchers suffered from was limitation of computational speed and data storage capacity which were restricted to employ fairly coarse numerical grids in calculations. This led to spatial oscillations in flow pattern and inaccuracy in results. Because of the rapid advancements design of powerful computers, this situation has changed in recent years. It is now possible to attempt simulating realistic unsteady flows by numerical methods.

The great advantage of a numerical simulation is the availability of details on all aspects of the flow for every stage of the flow development. In particular, in an experiment study in comparison to a numerical study, it is difficult to follow all of the details of transition flow form an initially quasi-steady flow to the final periodic vortex-shedding flow.

An early computer simulation at low Reynolds number was reported by Fromm & Harlow [17](1963). They study the development of a vortex street behind a plate which has impulsively accelerated to constant speed in a channel of finite width; the Reynolds-number range investigated was $15 \leq Re \leq 6000$, but a few results appeared in their paper. This simulation, although a major achievement at that time, was flawed by the use of central differencing at large cell Reynolds numbers.

Along the same lines, a more detailed study was performed by Davis and Moore [14] (1982). They employed a finite volume method and simulated two-dimensional time-dependent flows over rectangles in infinite domains. The numerical method used was a multi-dimensional version of the one-dimensional QUICKEST scheme proposed by Leonard [26] (1979). Average and RMS values of the lift and drag coefficients, as well as Strouhal number values, were computed for a square cylinder at three different angles of incidence over Reynolds number from 100 to 2800. Computed Strouhal numbers compare well with those obtained from a wind-tunnel test for Reynolds numbers below 1000. The difference were less than 10% in general.

Davis *et al.* [15] (1984) extended the numerical scheme of Davis & Moore (1982) to include the effects of confining walls. They concluded that the presence of walls leads to significant changes in the flow characteristics including increased drag coefficient and Strouhal number.

Nagano *et al.* [32] (1982) employed a discrete vortex method to extend the range of computations to higher Reynolds number (from 1×10^4 to 1×10^5) and aspect ratio ranging from .5 to 2. The results are about 10% higher than those obtained experimentally by Otsuki *et al.* [45] (1974). Their numerical results showed that the vortex shedding is locked to the vibration of the cylinder for a square cylinder in forced transverse vibration in the range of .9 to 1.04. Similar numerical results are also reported by Belotserkovsky *et al.* [5] (1993).

Along the same line Franke *et al.* [16] (1990) carried out a numerical calculations of laminar vortex-shedding flows past square cylinder $Re \leq 300$. The calculations were performed by solving the unsteady 2D Navier-Stokes with a finite volume method incorporating the third-order-accurate discretization scheme QUICK. They mentioned that their results show good agreement for the lower Reynolds numbers at which fully laminar flow can be expected. They explained that for this geometry, numerical problems are more severe owing to the extreme

velocity gradients prevailing at the sharp corners of the square cylinder. This may be responsible for the fact that numerical and experimental results do not compare satisfactorily in all details. They also explained that one problem common to most numerical studies of vortex-shedding flow past cylinders is the presence of numerical diffusion, which effectively reduces the Reynolds number and may even prohibit the self-excitation of vortex shedding. A trustworthy numerical method should be able to predict the occurrence of periodic vortex shedding by itself.

By the finite difference method, flow around cylinders with rectangular cross sections of various width-to-height ratios of .4 to 8 have been computed in the range of Reynolds numbers from 100 to 1200 by Okajima *et al.* [43] (1990). They explain that the component with a high Strouhal frequency is induced by the vortices separated from the trailing edges and that the flow Strouhal component is due to the oscillation of flow over the side surfaces accompanied by the movement of separation bubbles. A summary of their results is presented below.

1. At Reynolds number beyond 500, the flow around the cylinder with side ratio 2 becomes fully separated from the leading edges, while for the cylinder with the side ratio 2.8 and $Re = 1200$, a separated shear layer tends alternately to reattach onto cylinder surfaces to form the unsteady separation bubble. Two kinds of Strouhal components appear in the flow around the cylinder with side ratio 6 at Reynolds number 800.
2. It is shown that the critical side ratio of a rectangular cross section for which Strouhal number abruptly changes is about 2.8 or 6 at the Reynolds numbers of 500 to 1200.
3. For side ratio 6 at Reynolds number over 500, two Strouhal number are found to exist, one induced by the fluctuation of the unsteady separation bubble with the lower Strouhal number and the other by the vortices formed behind cylinder with higher Strouhal number.
4. The simulated results of the behavior of the vortices and separation bubble indicate that the Reynolds of about 400-500, where base pressure coefficient has a minimum, is the critical region in which the separation bubble fluctuates synchronizing with the motions of the wake in the case of cylinder with the side ratio over 6.

Tamura & Kuwahara [62] (1990) investigated the aerodynamics behavior of a cylinder in a uniform flow at high Reynolds number. They obtained the numerical solution for the unsteady flow by formulating the 2-D and 3-D incompressible Navier-Stokes equations in a generalized coordinate system. No turbulence models was incorporated and the third-order upwind scheme for the convection terms was adopted in their numerical procedure. In the case of 3-D computation, the periodic boundary condition was employed in the spanwise direction. Computational examples were the square cylinder with length-to-diameter ratios of 0 (2D), 1, 1.3 and 4. Through the comparison between 2-D and 3-D computational results, they clarified the 3-D effects on the aerodynamic properties of a square cylinder, such as the main and fluctuating aerodynamic forces and Strouhal numbers properties of a square cylinder. They explained that according to the computational results by Tamura *et al.* [61] (1988), even if a sufficiently large number of grid points are employed, there exist intrinsic disagreements between the two dimensional computational results and the experimental data. In particular, these discrepancies are conspicuous in the flow details around a bluff body at high Reynolds numbers. It can be attributed to the fact that 2-D turbulence has characteristics fundamentally different form those of the 3-D situations in the decay process. Consequently, they showed that 3-D flow structures have appreciable effects on the aerodynamic forces acting on the body. It may be difficult to predict the aerodynamic behavior accurately if one relies on the two dimensional flow calculations at high Reynolds number. Then, they concluded that the flow patterns obtained by 2-D Navier Stokes equations have significant differences from that by the 3-D, even for the case of 2-D problems. Especially in the near wake, 3-D structures gradually emerge by the vortex instability. These

flow characteristics have appreciable effects on the aerodynamic behavior. The computational results have revealed that 3-D structures decrease the averaged drag value and the lift amplitude. Hence the 3-D computational result of the cylinder with the long-length periodicity is closer to the experimental value, which is obtained by using the long span cylinder, than the 2-D results.

Along the above line, Tamura *et al.* [63] (1990) has questioned the reliability of 2D-calculations in turbulent flow. They applied the direct finite difference technique of the incompressible Navier-Stokes equations to unsteady flows around a rectangular cylinder and a circular cylinder. For high Reynolds number flows, the third-order upwind scheme was employed for convective terms without turbulence modeling. Two-dimensional structures in the wake were concluded to result in peculiar aerodynamics, and three-dimensional structures of wake flows was significant even for the two-dimensional problems concerned with a cylinder-type structure. They concluded that numerical predictions of the aerodynamics characteristics concerning the time-averaged as well as the unsteady data are essentially different between the two- and three-dimensional simulations. The two-dimensionally computed values of aerodynamic forces as a cylinder usually tend to indicate a conservative estimate for the structural design because of the very strong two-dimensional vortices.

Okajima [41] (1990) has calculated flows around rectangular cylinders in the range of low Reynolds numbers of 150 to 800 at zero incidence by a finite difference method and flows at high Reynolds numbers by a discrete vortex method to gain a better insight into the detailed flow characteristics. His results simulated by finite difference method successfully indicate the existence of the critical range of Reynolds number where the value of Strouhal number changes, accompanied with a drastic change of flow pattern. At high Reynolds numbers, he has computed flows around rectangular cylinders with different side ratios from .6 to 8 by discrete vortex method and succeed to capture the phenomenon that the value of Strouhal number abruptly changes when the side ratio of a model is 2.8 or 6, which are the critical values.

A little different but along the same line, it is seen the work of Arnal *et al.* [1] (1990). They investigated the characteristics of the flow around a bluff body of square cross-section in contact with a solid wall boundary numerically using a finite difference procedure. Previous studies have shown qualitatively the strong influence of solid-wall boundaries on the vortex shedding process and the formation of the vortex street downstream. In their study three cases were investigated which correspond to flow past a square rib in a freestream, flow past a rib on a fixed wall and flow past a rib on a sliding wall. Values of Reynolds number studied ranged from 100 to 2000, where the Reynolds number is based on the rib height and bulk stream velocity. Comparisons between the sliding-wall and fixed-wall cases show that the sliding wall has a significant destabilizing effect on the recirculation region behind the rib. Results show the onset of unsteadiness at a lower Reynolds number for the sliding-wall case ($50 \leq Re \leq 100$) than for the fixed-wall case ($Re \geq 100$). A careful examination of the vortex shedding process reveals similarities between the sliding-wall case and both the freestream and fixed-wall cases. At moderate Re ($Re \geq 250$) the sliding-wall results show that the rib periodically sheds vortices of alternating circulation in much the same manner as the rib in a freestream. The vortices are distributed asymmetrically downstream of the rib and are not of equal strength as in the freestream case. However, the sliding-wall case shows no tendency to develop cycle-to-cycle variations at higher Reynolds number, as observed in the freestream and fixed-wall cases. Thus, while the moving wall causes the flow past the rib to become unsteady at a lower Reynolds number than the fixed-wall case, it also acts to stabilize or "lock-in" the vortex shedding frequency. This is attributed to additional source of positive vorticity immediately downstream of the rib on the sliding wall.

The slightly different problem of flow stability has been approached by Kelkar & Patankar [23] (1992) to determine the Reynolds number at which flow around square cylinders at angles

of 0° becomes unsteady. They analyzed stability of the steady flow to small two-dimensional perturbations by computing the evolution of these perturbations. Then, an analysis of various time-stepping techniques was carried out to select the most appropriate technique for predicting the growth of the perturbations and hence the stability of the flow. Finally the critical Reynolds number was determined from the growth rate of the perturbations and computations were then made for periodic unsteady flow at a Reynolds number above the critical value.

Okajima *et al.* [44] (1992) have used a finite volume method to compute laminar flows around bluff bodies with a rectangular cross-section of various width-to-height ratios from .2 to 10. They used a cross-sections with a round leading edge or a square trailing edge at Reynolds number of $(1, 4, 7) \times 10^3$. Turbulent flows were also computed using a standard $k - \epsilon$ turbulence model. Computed results were compared with experimental data at a Reynolds number of 10^3 and clearly showed the effects of the shape of the bluff body on the aerodynamic characteristics. They could successfully simulate some interesting phenomena whereby the flow pattern changes critically when the side ratio is about 2.1 and 6; that was, a fully separated flow, an alternately reattached one and a stationarity reattached one. The results also revealed interactions between the wake and separation bubbles. There are, however, significant discrepancies between the results from the $k - \epsilon$ turbulence model and experiments.

The paper of Rodi [55] (1993) reviewed calculations performed to-date of vortex shedding flow past long cylinders at high Reynolds numbers where the effect of stochastic turbulent fluctuations superimposed on the 2D periodic shedding motion needs to be simulated. The experiences gathered with various statistical turbulence models ranging from algebraic eddy-viscosity models to Reynolds-stress equation models were summarized and discussed, and calculations were confronted with large-eddy simulations whenever possible, and a comparative discussion on the various calculation methods was given.

Zaki *et al.* [70] (1994) employed a finite-difference method for solving flow around a fixed-cylinder with cylinder orientation for Reynolds numbers up to 250. Most of the numerical results, which are appeared in paper of Zaki *et al.* relate to Reynolds number up to 50. Only variation of Strouhal number for zero angle of incidence with Reynolds number up to 250 is found in their paper.

The slightly different problem but in the same line is the work of Li & Humphrey [27] (1995). They studied the unsteady, two-dimensional flow and heat transfer due to a square obstruction located asymmetrically between the parallel sliding walls of a channel with length-to-height ratio 6.44. Laminar, constant property flow was assumed for the obstruction configurations in which the blockage ratio was .192, the nearest-wall distances are 0.2, 0.5 and 1, the orientation angles were 0° , 10° , and 20° and Reynolds numbers were $Re=100, 500, \text{ and } 1000$. They concluded that relative to a freestream flow or the flow in the channel with fixed walls, at the same Reynolds number, the sliding wall condition increases the drag experienced by a cylinder for all the values of orientation angles and the nearest-wall distances.

In previous work of Sohankar *et al.* [59], for the square cylinder at zero incidence, influence of time step, distribution of grid points, size of cells adjacent to the body, upstream and downstream extents of calculation domain and blockage were thoroughly investigated ($Re = 100$). Influence of Reynolds number ($Re = 45 - 250$) at blockage $\beta = 5\%$ was also presented. It was found that the results strongly depend on time step, grid, cell size, domain size, solid blockage and discretization scheme.

<i>Ref.</i>	<i>Re</i>	<i>B/A</i>	$\alpha[^\circ]$	$\beta(\%)$	X_d	X_u	<i>Method</i>
Davis & Moore [14]	100-2800	1	0-15	8.3	4.5	9.5	FD
Davis & Moore [14]	250, 1000	1.7	0, 90	8.3	4.5	9.5	FD
Franke <i>et al.</i> [16]	≤ 300	1	0	8.3	4.5	14.5	FV
Okajima <i>et al.</i> [43]	100-1200	1-8	0, 90	-	-	-	FD
Okajima [42]	150-800	1-8	0, 90	-	-	-	FD
Arnal <i>et al.</i> [1]	100, 500, 1000	1	0	-	-	-	FD
Patankar [23]	100	1	0	14	4	9	FV
Zaki <i>et al.</i> [70]	≤ 250	1	0-45	-	-	-	FD
Sohankar <i>et al.</i> [59]	40-250	1	0	2-7	7-18	10-56	FV

Table 1: Comparison between employed numerical parameters for different researchers

5 Numerical Procedures

The flow is assumed to be two-dimensional, unsteady, incompressible and viscous. An incompressible SIMPLEC finite volume code, CALC-BFC (Boundary Fitted Coordinates), is used employing non-staggered grid arrangement for calculating the flow around a body by solving the continuity and the Navier-Stokes equations. The scheme is implicit in time, and a Crank-Nicolson scheme which is of second order has been used. The convective terms are discretized using either the third-order QUICK differencing scheme [26] or the second-order scheme of van Leer [65, 66]. The diffusive terms are discretized using central differencing, which is of second order accuracy. More details of the code and equations are described in the following.

6 Equations

6.1 General Transport Equation

The general transport equation in Cartesian coordinates for a variable Φ reads:

$$\frac{\partial \rho \Phi}{\partial \tau} + \frac{\partial}{\partial x_m} (\rho U_m \Phi) = \frac{\partial}{\partial x_m} \left(\Gamma_\Phi \frac{\partial \Phi}{\partial x_m} \right) + \bar{S}^\Phi \quad (1)$$

where \bar{S}^Φ denotes the source per unit volume for the variable Φ . Define a flux vector J_m containing convection and diffusion as follows:

$$J_m = \rho U_m \Phi - \Gamma_\Phi \frac{\partial \Phi}{\partial x_m} \quad (2)$$

Integration over a typical control volume with volume V and surface A , using the Gauss' law yields:

$$\int_V \frac{\partial \rho \Phi}{\partial \tau} dV + \int_A \mathbf{J} \cdot d\mathbf{A} = \int_V \bar{S}^\Phi dV \quad (3)$$

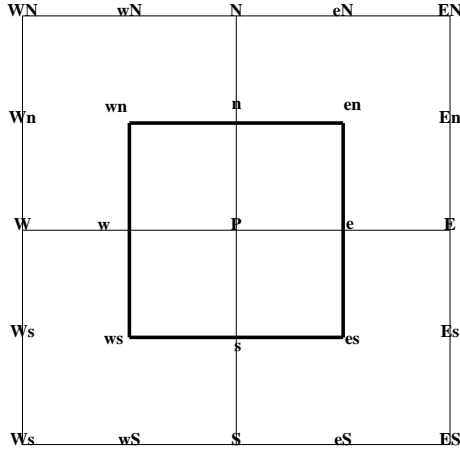


Figure 2: Grid nomenclature. The grid is drawn using Cartesian coordinates for clarity. Bold lines construct a typical control volume.

6.2 Mean Flow Equations

The incompressible continuity equation and the unsteady momentum equation read

$$\frac{\partial U_i}{\partial x_i} = 0 \quad (4)$$

$$\rho \frac{\partial U_i}{\partial \tau} + \rho \frac{\partial}{\partial x_j} (U_i U_j) = -\frac{\partial p}{\partial x_i} + \mu \frac{\partial^2 U_i}{\partial x_j \partial x_j} \quad (5)$$

7 The Code

7.1 Basics

In this section, the finite volume computer program CALC-BFC (Boundary Fitted Coordinates) for three-dimensional complex geometries is presented. The code is described in [13], and its main features are given below for convenience. The program uses Cartesian velocity components, as have been used by e.g. Shyy *et al.* [58] and Braaten and Shyy [10]. In most finite volume programs, staggered grids for the velocities have been used [23]. In the present work collocated variables are used, which means that velocities are stored at the same place as all scalar variables such as p, k, ε . This concept suggested by Rhie and Chow [53] has been used, for example, by Burns and Wilkes [11], Peric *et al.* [51], Miller and Schmidt [29].

Equation 3 is discretized using standard control volume formulation as described in Patankar [50]. The integration of Eq. 3 over a control volume (See Fig. 2) gives:

$$(\mathbf{J} \cdot \mathbf{A})_e + (\mathbf{J} \cdot \mathbf{A})_w + (\mathbf{J} \cdot \mathbf{A})_n + (\mathbf{J} \cdot \mathbf{A})_s = S^\Phi \delta V$$

Note that the positive signs on the terms containing contributions from west and south surfaces will be negative because these scalar products in themselves are negative.

The discretized equation will be of the form:

$$a_P \Phi_P = \sum a_{nb} \Phi_{nb} + S_C^\Phi \quad (6)$$

where

$$a_P = \sum a_{nb} - S_P^\Phi$$

The coefficients a_{nb} contain contributions due both to convection and diffusion, and the source terms S_C^Φ and S_P^Φ contain the remaining terms.

7.2 Convection

The convection which is the first part of the flux vector \mathbf{J} , is the scalar product of the velocity vector and the area vector multiplied by the density. For an east face it gives:

$$\dot{m} = \rho \mathbf{U} \cdot \mathbf{A} = \rho_e (U_e A_{ex} + V_e A_{ey})$$

and since the Cartesian areas A_{ex} , A_{ey} are stored in the program, the calculation of the convective contributions to \mathbf{J} is straightforward. Special care must, however, be taken to avoid non-physical oscillations when the velocities are interpolated from their storage location at the cell center to the control volume faces. Rhie and Chow [53] solved this problem.

Calculation of the velocities at control volume faces is described below. For simplicity, Cartesian coordinates are used. When the pressure gradient is added to the momentum equation, standard linear interpolation is used, i.e.

$$\left(\frac{\partial p}{\partial x} \right)_P = \frac{p_e - p_w}{|\mathbf{we}|}$$

where

$$p_e = f_x p_E + (1 - f_x) p_P$$

When calculating the velocity at the east face, for example, the pressure gradient is subtracted so that

$$U_P^\# = U_P - \frac{-(p_e - p_w) \delta V}{|\mathbf{we}| (a_P)_P}$$

$$U_E^\# = U_E - \frac{-(p_{Ee} - p_e) \delta V}{|\mathbf{e}(\mathbf{Ee})| (a_P)_E}$$

where a_P is the discretized coefficient in the U -momentum equations (see Eq. 6). The U -velocity at the east face of the control volume is now calculated as:

$$U_e = f_x U_E^\# + (1 - f_x) U_P^\# - \frac{(p_E - p_P) \delta V}{|\mathbf{PE}| (a_P)_e}$$

The advantage of the last expression is obvious: now the pressure gradient is calculated using the adjacent nodes of face e . This prevents non-physical oscillations in the pressure field.

7.3 Diffusion

Diffusion is the second part of the flux vector \mathbf{J} in Eq. 2, and it has the form:

$$\mathcal{D} = (\mathbf{J} \cdot \mathbf{A})_{diff} = -\Gamma_\Phi \mathbf{A} \cdot \nabla \Phi$$

For the east face, for instance, it gives in Cartesian coordinates (x, y)

$$-\{\Gamma_\Phi \mathbf{A} \cdot \nabla \Phi\}_e = -\left\{ \Gamma_\Phi \left(A_x \frac{\partial \Phi}{\partial x} + A_y \frac{\partial \Phi}{\partial y} \right) \right\}_e$$

and in curvilinear coordinates (ξ, η)

$$-\{\mathbf{A} \cdot \nabla \Phi\}_e = -\left\{ \mathbf{A} \cdot \mathbf{g}_i g^{ij} \frac{\partial \Phi}{\partial \xi_j} \right\}_e = -\left\{ |\mathbf{A}| \mathbf{n} \cdot \mathbf{g}_i g^{ij} \frac{\partial \Phi}{\partial \xi_j} \right\}_e \quad (7)$$

The covariant (= tangential) base vectors $\mathbf{g}_1, \mathbf{g}_2$ correspond to the I, J grid lines, respectively. The metric tensor is involved because the components of the product $\mathbf{A} \cdot \mathbf{g}_i$ and the derivative $\partial \Phi / \partial \xi_j$ are both covariant, and the product of their (contravariant) base vectors is not equal to zero or one (as in Cartesian coordinate systems) since they are non-orthogonal to one another.

The normal vector in Eq. 7 is equal to the cross product of \mathbf{g}_2 and \mathbf{g}_3 ($\mathbf{g}_3 = \mathbf{e}_z = (0, 0, 1)$ since it is a two-dimensional configuration), i.e.

$$\mathbf{n} = \mathbf{g}_2 \times \mathbf{g}_3 \equiv \mathbf{g}^1$$

which from $\mathbf{g}_i \mathbf{g}^j = \delta_i^j$ gives

$$\mathbf{n} \cdot \mathbf{g}_2 = 0.$$

Equation (7) can now be written

$$\begin{aligned} -\{\mathbf{A} \cdot \nabla \Phi\}_e &= -\left\{ |\mathbf{A}| \mathbf{n} \cdot \mathbf{g}_1 g^{1j} \frac{\partial \Phi}{\partial \xi_j} \right\}_e \\ &= -\left\{ |\mathbf{A}| \mathbf{n} \cdot \mathbf{g}_1 \left(g^{11} \frac{\partial \Phi}{\partial \xi} + g^{12} \frac{\partial \Phi}{\partial \eta} \right) \right\}_e. \end{aligned}$$

The diffusive terms are discretized using central differencing, which is of second order accuracy [50].

7.4 Pressure Correction Equation

The discretized continuity equation in one dimension takes the form:

$$\dot{m}_e - \dot{m}_w = 0 \quad (8)$$

where \dot{m} denotes the mass flux, which is calculated as

$$\dot{m} = \rho \mathbf{A} \cdot \mathbf{U}$$

In SIMPLEC [50], the mass flux is divided into one old value \dot{m}^* and one correction \dot{m}' to the old one, so that

$$\dot{m} = \dot{m}^* + \dot{m}'$$

and the covariant velocity components are related to the pressure gradient as

$$V_i = -\frac{\delta V}{a_P} \frac{\partial p}{\partial x_i} \quad (9)$$

where a_P comes from the discretized U_i -equation (see Eq. 6). The mass flux correction at the east face can now be obtained as:

$$\dot{m}'_e = (\rho \mathbf{A} \cdot \mathbf{U}')_e = \rho_e (A_{ex} U'_e + A_{ey} V'_e) = (\rho \mathbf{A} \cdot \mathbf{g}^j V'_j)_e$$

Using Eq. 9 gives

$$\dot{m}'_e = \left\{ \rho \mathbf{A} \cdot \left(-\frac{\delta V}{a_P} \frac{\partial p'}{\partial x_j} \mathbf{g}^j \right) \right\}_e = - \left(\frac{\delta V \rho}{a_P} \mathbf{A} \cdot \nabla p' \right)_e = 0 \quad (10)$$

where p' is the pressure correction. Equations 8 and 10 give

$$\left(\frac{\delta V \rho}{a_P} \mathbf{A} \cdot \nabla p' \right)_w - \left(\frac{\delta V \rho}{a_P} \mathbf{A} \cdot \nabla p' \right)_e + \dot{m}_e^* - \dot{m}_w^* = 0$$

This equation is a diffusion equation for the pressure correction p' .

8 Boundary Conditions

The inlet is placed some body heights upstream of the body, see Fig. 3, where $U = 1$, $V = 0$ is prescribed. At the outlet, the U -velocity is calculated from global continuity together with a zero gradient boundary condition for both U and V . No-slip conditions are prescribed at the body surfaces ($U = V = 0$). At the upper and lower boundaries symmetry conditions simulating a frictionless wall are used ($V = \frac{\partial U}{\partial y} = 0$). The second normal derivative for the pressure is set to zero at all boundaries. The time-marching calculations are started with the fluid at rest, after which the inlet velocity is increased to unity in two time units by a sine function.

9 Results and Discussion

An extensive investigation of the influence of computation parameters such as time step, near- and far-field resolution, distribution of grid nodes and domain sizes, as well as the influence of physical parameters such as Reynolds number, cylinder side ratio and angle of incidence was performed. In the fully saturated state, i.e. at physical times when memory effects of the starting process are negligible, many useful physical quantities were computed, for example, dominating wake frequency, mean and RMS values for various wall pressures, lift, drag and moments, respectively. In addition, for some selected cases, sequences of flow patterns within this saturated state are presented.

All sensitivity studies on the influence of numerical parameters (including blockage) were carried out for the square cylinder, $B/A = 1$. Except for the influence of Δ , i.e. the far-field resolution, some results of this separate investigation have previously been reported [59]. The cylinder then was set at zero angle of incidence with $Re = 100$.

Except otherwise stated, the following numerical parameters (including blockage) were used:

Δt	δ	Δ	X_u	X_d	β	Scheme
0.025	0.004	0.5	11.1	25.2	5%	QUICK

Below, the reasons for choosing this set of parameters are discussed.

9.1 Influence of Time Step

Obviously, the time step in the time-marching calculations of vortex shedding flow is an important parameter. If too large values are chosen, the global and phase accuracy may be seriously affected. When considering aspects of both accuracy and CPU-time, a non-dimensional time step of $\Delta t = 0.025$ was found to be reasonable. This value was also chosen by Franke and Rodi [16]. When decreasing the time step to 0.02 the effects were considered to be of minor importance, especially so for the Strouhal number and the mean drag coefficients, see Table 2. Please note that the number of time steps within one period of shedding is equal to $(\Delta t St)^{-1}$ which means that $\Delta t = 0.025$ in Table 2 corresponds to about 275 points per period.

Table 2 also pinpoints to the general observation that quantities which are directly related to the dynamic flow situation, e.g. fluctuating lift and drag, generally are more sensitive to variations in numerical parameters than global mean quantities such as Strouhal number and mean drag. As validated further below, among the various quantities which were calculated, the RMS lift coefficient probably is the best overall indicator. For example, when considering Strouhal number and mean drag only, the case at $\Delta = 0.05$ seems satisfactory. However, other quantities such as the RMS lift reveal the significant inaccuracies involved at this time step.

9.2 Influence of Grid and Cell Size

Distribution of grid points in non-uniform grids, for example, by the hyperbolic tangent and the hyperbolic sine functions, are discussed by Thompson *et al.* [64]. The hyperbolic sine gives a more uniform distribution in the immediate vicinity of the minimum spacing, and thus has less error in this region, but the hyperbolic tangent has the better overall distribution. The

Δt	St	C_D	$C_{D,p}$	$C_{p,f}$	$C_{L'}$	$C_{D'}$	$-C_{p,tb}$	$-C_{p,b}$	$C_{p,s}$	L_r
.050	.144	1.438	1.393	.728	.117	.0018	1.052	.649	1.040	2.72
.025	.145	1.444	1.398	.726	.130	.0019	1.063	.659	1.040	2.22
.020	.146	1.448	1.402	.726	.132	.0022	1.066	.661	1.040	2.20

Table 2: Effect of time step Δt for $B/A = 1$, $Re = 100$, $\alpha = 0^\circ$ ($\Delta = 0.7$).

Δ	α	<i>grid</i>	St	C_D	$C_{L'}$	$C_{D'}$
0.5	0°	126×96	0.168	1.439	0.227	0.013
0.3	0°	177×122	0.144	1.543	0.520	0.028
0.2	0°	348×224	0.149	1.445	0.362	0.020
0.5	20°	122×90	0.196	1.761	0.664	0.159
0.3	20°	185×135	0.196	1.796	0.707	0.175
0.5	45°	120×88	0.205	1.944	0.729	0.100
0.3	45°	182×133	0.204	2.022	0.790	0.083

Table 3: Effect of maximum cell size Δ for $Re = 200$, $B/A = 1$, $X_d = 26$, $X_u = 10$ and $\beta = 5\%$.

important point is that the spacing must not be allowed to change too rapidly in high gradient regions. After some testing, it was decided to use the hyperbolic tangent with a non-uniform grid extending 5 units upstream, downstream and sideways from the body. Beyond that the grid distribution was made uniform with a constant cell size variable between 0.2 – 0.7 length units (Δ).

For accurate calculations, the size of the cells adjacent to the cylinder should be sufficiently small. Wall distances for the near-wall node (δ) in between 0.001 and 0.005 units were investigated. For most of the results in this paper, the value 0.004 was used. Decreasing it to 0.001 gave negligible changes in the results. When decreasing δ and at the same time keeping a smooth distribution of nodes, the numbers of nodes must be increased.

We have also found that even if the cells far from the cylinder can be substantially larger than those close to the cylinder, the size of the former cells should not be too large. We have investigated the influence of grid and cell size in regions far from the cylinder for different angles of incidence at $Re = 200$. The required size of cells far from the body depends on the angle of incidence, as shown in Table 3. For Δ from 0.3 to 0.5 the greatest changes in values of Table 3 were found at zero incidence and appear in RMS lift. For example, this difference for the angles of incidence 0° , 20° and 45° are 150%, 6.5% and 8%, for RMS lift and -14%, 0%, 0%, for the Strouhal number, respectively. We see that the results at $\alpha = 0^\circ$ are much more dependent on the far field and distribution than at $\alpha \geq 20^\circ$. This may be because of increasing instability with increasing angle of incidence.

Please note that, as in the previous subsection, the RMS lift coefficient is much more sensitive to the numerical resolution than the Strouhal number.

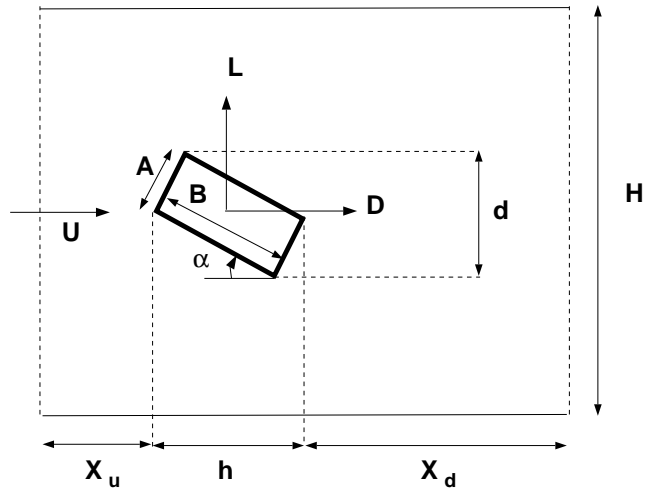


Figure 3: Domain of calculation

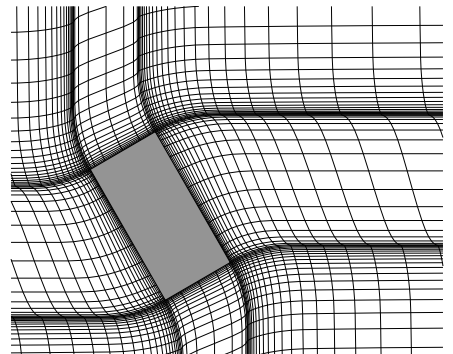
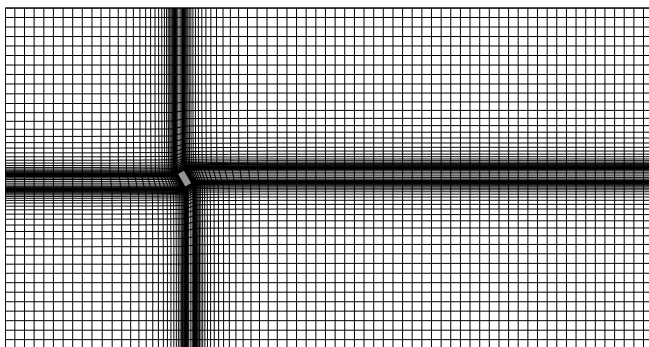


Figure 4: The 115×92 non-uniform grid for $B/A = 2$ and $\alpha = 60^\circ$: a) Domain of calculation; b) Near the cylinder surface.

9.3 Influence of Courant (CFL) Number

This fundamental stability condition of most explicit schemes expresses that the distance covered during the time interval Δt , by convection speed U , should be lower than the minimum distance between two mesh points ($U \Delta t / \Delta x \leq 1$). This is called the convection Courant number (CCFL) and this condition applies, generally, to explicit schemes for hyperbolic partial differential equations. In other words, the numerical scheme defining the approximation at each mesh point must be able to include all the physical information which influences the behavior of the system at this point, or a particle of fluid should not travel more than one spatial step-size in one time step.

Another form of CFL is called diffusion Courant number, DCFL ($\Delta t / (Re \Delta x^2) \leq 1$), which expresses how viscosity diffuses in the domain in comparison to the distance between two mesh points. By calculating CCFL and DCFL in the x and y direction, we find that maxima values of CCFL are about 8 ($Re = 100$). The maximum values of DCFL are 7.81 ($Re = 200$) and are located near the body. It is important to know that the time discretization in our study is implicit and high values of CFL do not influence on the stability of our scheme. The accuracy, however, can be affected. The finer mesh and the finer time steps should be used in order to keep CFL constant. This will be further studied in the near future.

9.4 Influence of Upstream Extent of Calculation Domain

The influence of the extent of the calculation domain upstream of the cylinder (X_u) was investigated and some results are listed in Table 4 (square cylinder at zero incidence, $Re = 100$). It should be stressed that when increasing the calculation domain from, for example, $X_u = 5$ to 11, the two grids are identical from 5 upstream of the body and downstream. When creating the grid with $X_u = 11$ from the grid with $X_u = 5$, cells with constant $\Delta x = 0.7$ are added (0n downstream side $\Delta x = 0.5$).

The grids were also created in the same way when investigating the influence of the calculation downstream of the cylinder and the blockage effect below. As can be seen from Table 4 a value of $X_u = 7.5$ has a large effect on the calculated results. On the other hand, an increase from $X_u = 11.1$ to 18.3 only gave minor changes. Thus we can conclude that the extent of the calculation domain upstream of the cylinder should be at least $X_u = 11$. Fig. 5 shows the time averaged pressure coefficient and U velocity along the centerline for different X_u . It can be seen that if X_u is larger than about 11, then the results are not affected if the distance is further increased.

As shown in Table 4, with X_u from 7.5 to 11.1, the most significant changes in values are in the RMS lift, stagnation pressure and frontal pressure coefficients which are decreased by 10, 3 and 3 percent, respectively. It is important to emphasize that the values of frictional lift and drag are approximately constant for all values of X_u and only the pressure forces change.

9.5 Influence of Downstream Extent of Calculation Domain

In Table 5 and Figs. 6 and 7 the influence of the downstream extent is depicted (square cylinder at zero incidence, $Re = 100$). These results show that in order to obtain results independent of the outlet, the extent of the calculation domain downstream of the cylinder must be as large as $X_d = 30$. A further increase to $X_d = 56.3$ did not produce any significant effects. It should be stressed that when increasing the calculation domain from, for example, $X_d = 14.9$ to 20, the

X_u	St	C_D	$C_{D,p}$	$C_{p,f}$	$C_{L'}$	$C_{D'}$	$-C_{p,tb}$	$-C_{p,b}$	$C_{p,s}$	L_r
7.5	.151	1.509	1.462	.727	.160	.0026	1.139	.720	1.055	2.08
11.1	.150	1.486	1.439	.705	.145	.0036	1.137	.723	1.027	2.08
18.3	.150	1.483	1.436	.699	.146	.0037	1.138	.725	1.021	2.06

Table 4: Effect of upstream extent for $Re = 100$, $X_d = 14.9$, $\beta = 7.1\%$, $\Delta = 0.7$ and $\alpha = 0^\circ$.

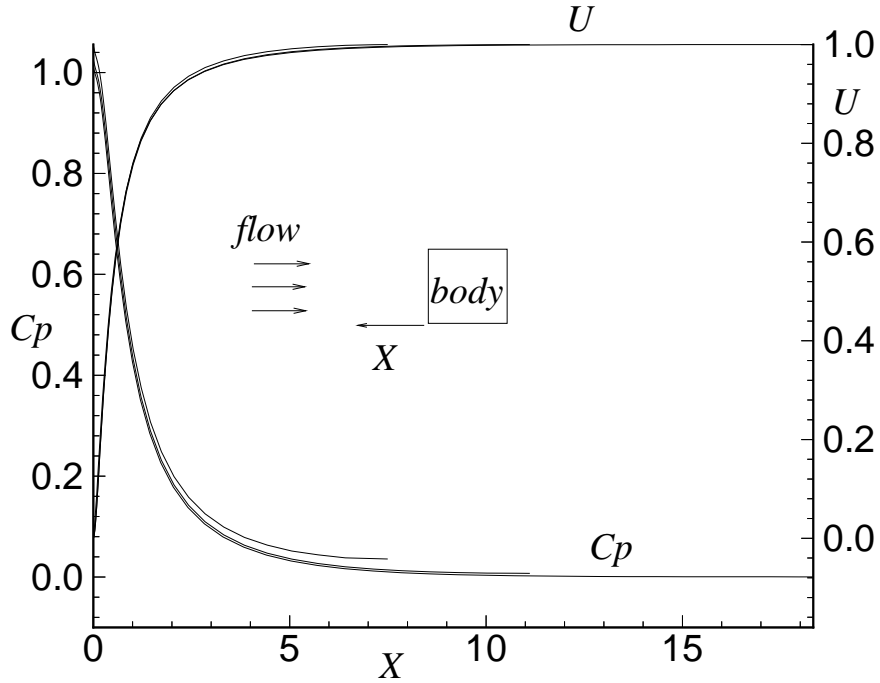


Figure 5: Mean pressure coefficient and velocity along the centerline for various location of inlet boundary X_u for $B/A = 1$, $\alpha = 0^\circ$, $Re = 100$, $X_d = 14.9$, $\beta = 7.1\%$.

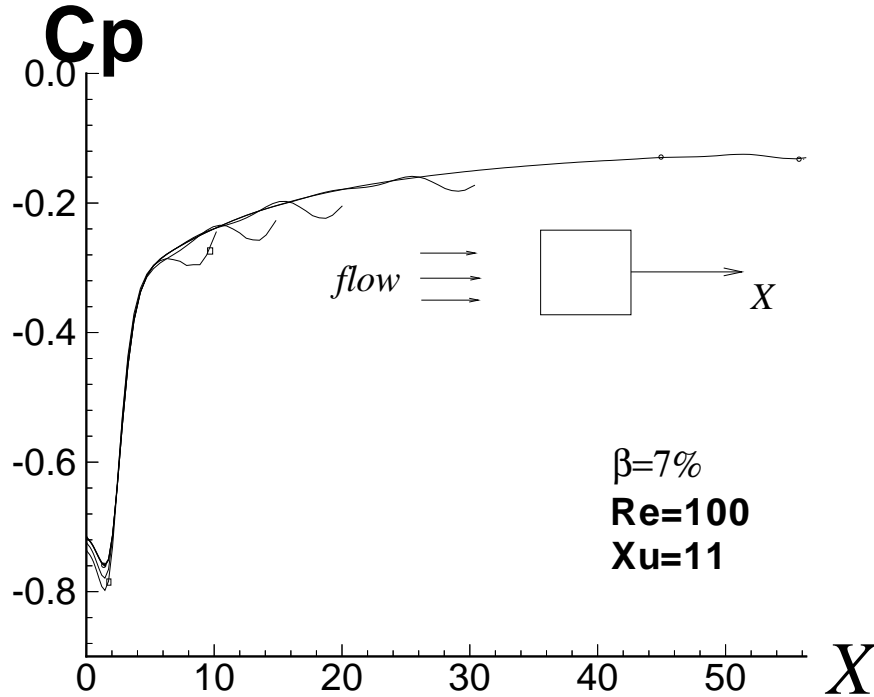


Figure 6: Time averaged pressure coefficient along the centerline

two grids are identical from 14.9 units downstream of the body and further downstream. When creating the grid with $X_d = 20$ from the grid with $X_d = 14.9$, cells with a constant $\Delta x = 0.7$ (downstream $\Delta x = 0.7$) added. The most important changes in values of Table 5 are in the lift coefficient, length of eddy and pressure base coefficient, where the changes are 54%, 13% and 3%, respectively, when X_d increases from 10.2 to 30.4. The majority of this differences occur between $X_d = 10.2$ and $X_d = 14.9$ where the corresponding changes are 10%, 5% and 1% respectively. A scrutiny of the downstream ends in Figs. 6 and 7 gives better understanding of these results. A change is seen at the end of each curve, which is caused by the influence of the outlet boundary condition. When X_d is not sufficiently large, the global flow pattern is affected thus causing changes in both pressure and velocity around the body. On the other hand, if X_d is sufficiently large the upstream influence from the outlet is effectively dampened out. In the present study, the commonly used boundary condition of zero streamwise gradients is used. Other boundary conditions which allow for a smoother discharge of the vortex street will be tested in the future.

9.6 Influence of Solid Blockage

The influence of solid blockage was investigated for the square cylinder at zero incidence ($Re = 100$). The blockage parameter was varied by changing the equal extent of the calculation domain above and below the cylinder. In the present work the upper and lower boundaries are treated as friction-free walls, i.e symmetry boundaries. The influence of blockage is presented in Tables 6 and 7 and Fig. 8. The QUICK scheme is unbounded and can give unphysical oscillations and

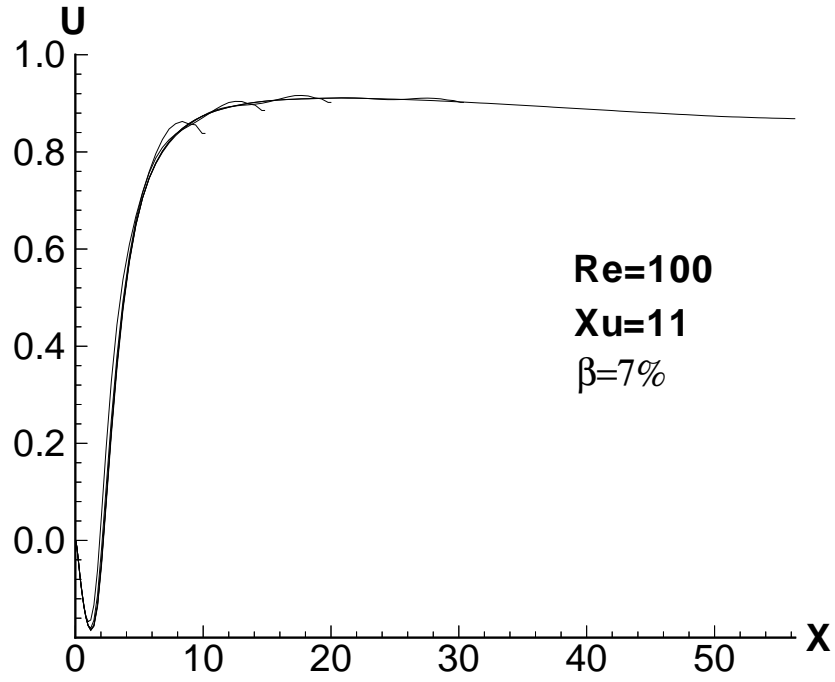


Figure 7: Time averaged velocity along the centerline

X_d	St	C_D	C_{D_p}	$C_{p,f}$	$C_{L'}$	$C_{D'}$	$-C_{p,tb}$	$-C_{pb}$	C_{ps}	L_r
10.2	.150	1.503	1.454	.703	.082	.0059	1.151	.735	1.027	1.90
14.9	.150	1.486	1.439	.705	.145	.0036	1.137	.723	1.027	2.08
20.0	.148	1.478	1.433	.706	.135	.0022	1.127	.714	1.027	2.20
30.4	.149	1.483	1.436	.706	.129	.0022	1.129	.715	1.027	2.18
56.3	.149	1.483	1.436	.706	.129	.0022	1.129	.715	1.027	2.18

Table 5: Effect of downstream extent for $B/A = 1$, $\alpha = 0^\circ$, $Re = 100$, $\Delta = 0.7$, $\beta = 7.1\%$.

β	St	C_D	C_{D_p}	$C_{p,f}$	$C_{L'}$	$C_{D'}$	$-C_{p,tb}$	$-C_{pb}$	C_{ps}	L_r
7.1	.142	1.466	1.425	.719	.127	.0023	1.106	.697	1.026	2.34
5.0	.139	1.423	1.382	.729	.130	.0025	1.042	.644	1.028	2.30
3.7	.136	1.401	1.360	.732	.129	.0029	1.006	.613	1.033	2.32
2.0	.135	1.390	1.348	.742	.122	.0044	0.971	.585	1.045	2.30

Table 6: Effect of blockage for $B/A = 1$, $\alpha = 0^\circ$, $Re = 100$, $X_d = 22.65$, $X_u = 18.3$, $\Delta = 0.7$ (van Leer scheme).

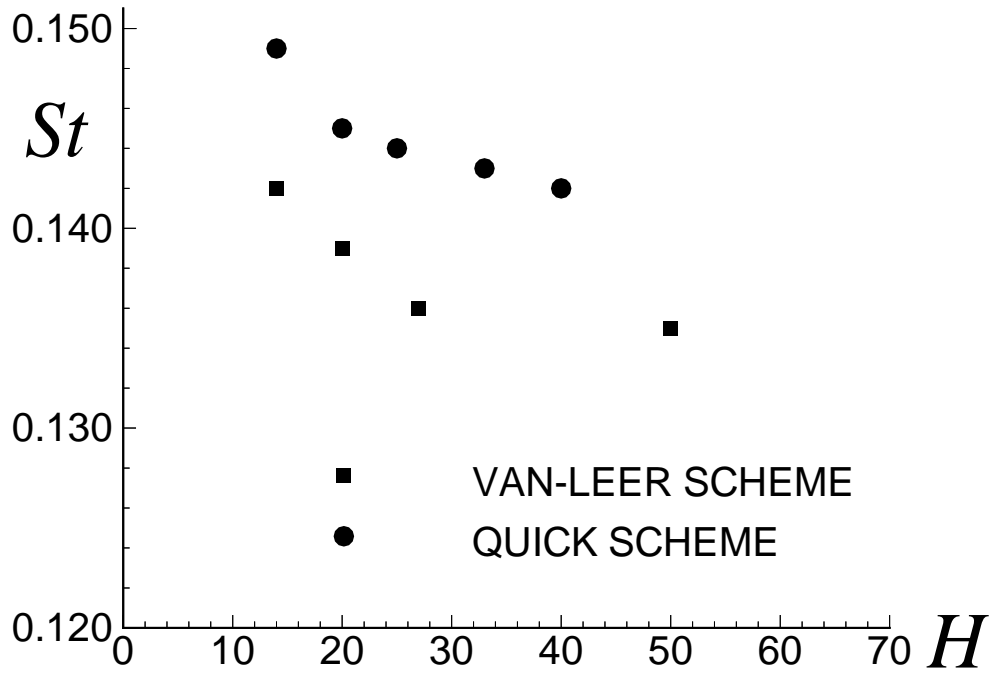


Figure 8: The effect of blockage ($\beta = d/H$) on Strouhal number for $Re = 100$, $X_d = 22.65$, $X_u = 18.3$, $\Delta = 0.7$.

β	St	C_D	C_{D_p}	$C_{p,f}$	$C_{L'}$	$C_{D'}$	$-C_{p,tb}$	$-C_{pb}$	C_{ps}	L_r
7.1	.149	1.481	1.435	.706	.129	.0024	1.128	.714	1.027	2.19
5.0	.145	1.444	1.398	.726	.130	.0019	1.063	.659	1.040	2.22
4.0	.144	1.434	1.388	.740	.133	.0026	1.035	.633	1.051	2.23
3.0	.143	1.431	1.386	.741	.142	.0020	1.020	.619	1.060	2.23
2.5	.142	1.432	1.386	.755	.147	.0014	1.015	.614	1.065	2.23

Table 7: Effect of blockage for $B/A = 1$, $\alpha = 0^\circ$, $Re = 100$, $\Delta = 0.7$

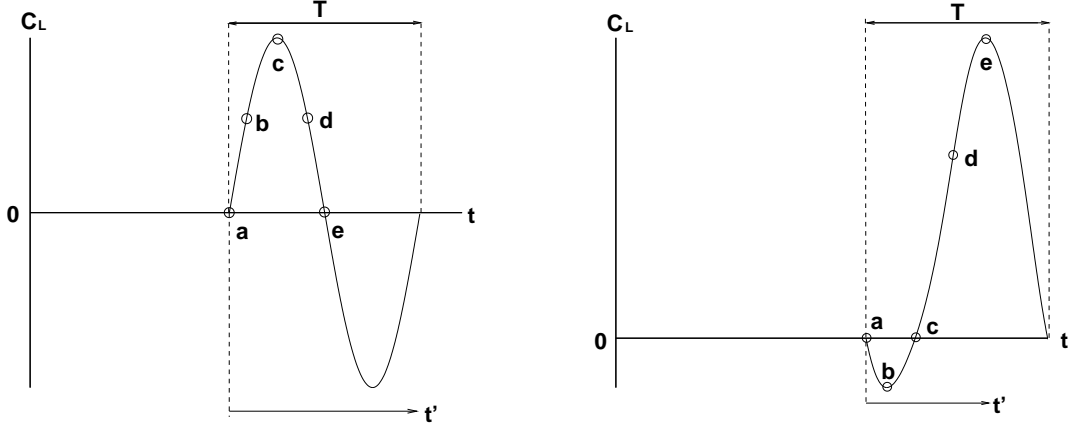


Figure 9: Location of sequence streamlines in Figs. 11 to 13 a) $Re = 75$ and 200 , $\alpha = 0^\circ$; b) $Re = 200$, $\alpha = 30^\circ$, $B/A = 2$

this actually occurred when the blockage was decreased to 2 percent. For this reason it was decided to use the more stable, bounded van Leer scheme in some additional calculations at low blockages. By comparing Tables 6 and 7 for $Re = 100$, the differences when using the two schemes are seen. Due to less accuracy, the Van-Leer scheme predicted lower values than the QUICK scheme. As can be seen from Tables 6 and 7, the results change even when using such small blockage as 2 percent. What is a bit surprising is that when the blockage is decreased from 3.7 percent to 2 percent, the lift coefficients change considerably. This may be due to numerical problems which are more effective in QUICK scheme than van Leer scheme. In Fig. 8, the blockage effects on Strouhal number are depicted. As can be seen, by decreasing the blockage (increasing height of domain) the Strouhal number decreases and we can expect that this reaches asymptotically a constant value for both schemes when the blockage reaches zero. As mentioned, the difference between the results for the two schemes is probably due to the QUICK scheme being more accurate than the van Leer scheme. But the two schemes show the same behavior for the blockage effect.

9.7 Flow Dynamics

Instantaneous streamlines, during half a period of vortex shedding in the fully developed state, for the square cylinder at zero incidence and for $Re = 75$ and $Re = 200$ are shown in Figs. 11 and 12. Fig. 13 shows a similar sequence of flow patterns for $Re = 200$ ($\alpha = 30^\circ$). For $\alpha = 0^\circ$ the flow is symmetric and thus we only present the flow during half a period, see Figs. 9, 11 and 12. The streamlines in Figs. 11 - 13 are presented at time locations corresponding to the lift coefficient, see Fig. 9.

In the flow around a rectangular cylinder, the sharp corners are natural points of separation. It was found [59] that the separation points for the square cylinder at zero angle of incidence are located at the rear corners for Reynolds number less than 125 (see Fig. 12). By increasing the Reynolds number, the separation points move along the side surfaces from rear corner towards the frontal corners, see Fig. 11. At a Reynolds number of about 125, a small back-flow region is observed at the top and bottom of the body and this region is larger at higher Reynolds number.

As shown in Fig. 9a, the cases in Figs. 11 and 12 which are marked a , c and e , respectively,

corresponds to zero (increasing), maximum and zero (decreasing) lift ($t'/T = 0, 0.25, 0.5$). For the case in Fig. 13 the points at zero (decreasing), minimum, zero (increasing) and maximum lift are marked a, b, c and e , respectively, see Fig. 9b. Finally, in Figs. 11 - 13 the cases marked f shows the time average streamlines in one period (T) of vortex shedding. At $t'/T = 0$ ($Re = 75$, $T = 7.5$) there is a clockwise vortex in development at the upper base corner, being fed by the separation at that very corner. As it grows, with increasing strength but being rather fixed in position, the attachment point on the rear side is being pushed downwards, see Fig. 11a-c. As the attachment point reaches the lower base corner, in between Fig. 11c and d, the lift already has passed its maximum level and a new anti-clockwise vortex is about to be formed at that very corner, which thereafter feeds its circulation. As this new vortex grows, see Fig. 11d and e, the old clockwise vortex is being pushed away and is eventually shed into the wake. In general terms, the same trend occurs at $Re = 200$ ($T = 6.1$) but the main difference between these two time sequences is due to the fact that for $Re = 200$, separation occurs at the frontal corners which causes reverse flow at the top and bottom of the body. In Fig. 13 streamlines around a rectangular cylinder with side ratio $B/A = 2$ and $\alpha = 30^\circ$ are shown for a Reynolds number of 200, in one period of shedding. In the first figure, which corresponds to zero lift, two vortices can be seen which are formed, at the windward lower corner and at leeward lower corner, respectively. Both vortices have positive vorticity (anti-clockwise). In Fig. 13b, these two vortices merge together to form a bigger vortex which is then shed in the wake, as is seen in Fig. 13c. At the same time another vortex forms at the leeward upper corner which then becomes bigger and rolls down on the leeward surface and finally is shed in the wake.

Fig. 10 shows the time history of drag, lift and moment for $Re = 200$, $B/A = 2$ and $\alpha = 60^\circ$. As the time-marching process is started, the time history of forces and moment pass a transient start-up process to the fully periodic stage. For example, this transition part for Fig. 10 is about 20 units of time. This transition part depends on the Reynolds number, the side ratio and the angle of incidence. By increasing the Reynolds number, the angle of incidence and decreasing the side ratio, the transition time sharply decreases as the instabilities of the flow increase. For example, by increasing the Reynolds number from 100 to $Re = 200$ ($B/A = 1$, $\alpha = 0^\circ$) the transition time is reduced by about 50 percent. By increasing the angle of incidence from 0° to 45° ($Re = 200$, $B/A = 4$) the transition time is reduced by 15 percent and at $\alpha = 90^\circ$ this time is half of that at $\alpha = 0^\circ$.

9.8 Influence of Side Ratio

In Fig. 14 values of C_D , St and C_L vs. projected side ratio h/d at $Re = 100, 200$ (blockage $\beta = d/H = 5\%$) are shown together with experimental results as given by Okajima [40, 42]. Considering the experimental uncertainties, the possible effects of end conditions and the effects due to numerical factors, the agreement seems satisfactory. Interestingly, there was no indication of a local maximum in the drag coefficient at some intermediate critical side ratio. In turbulent flow, such a maximum occurs at around $h/d = 0.6$, see e.g. [33, 4, 35]. Probably, this phenomenon is related to an interaction between the separated shear layers and the downstream part of the body, see e.g. [43, 39]. Although not fully investigated at present, this type of shear layer/edge interaction does not seem to occur in laminar vortex shedding flow. The vortex shedding strength shows a drastic decrease with increasing h/d . For instance, at $Re = 100$, the RMS lift coefficient at $h/d = 2$ is about 3 times lower than at $h/d = 1$.

The Strouhal number for $Re = 100$ decreases smoothly by side ratio but for $Re = 200$ it increases rather abruptly at around $h/d = 2$. At $h/d \geq 2$ for $Re = 200$ the flow reattaches on the longest side which not is the case at $h/d < 2$. In other words, for $Re = 100$ with different side ratios,

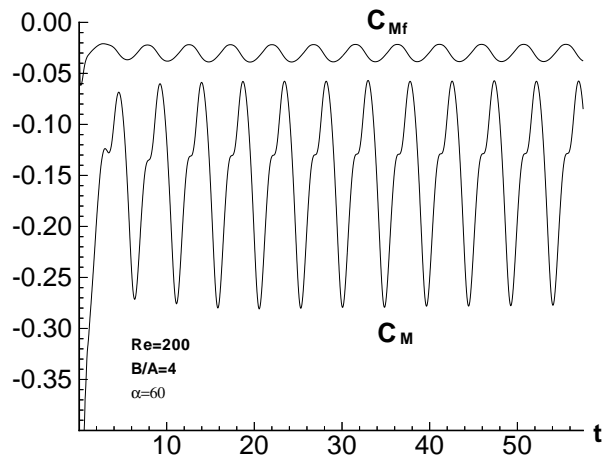
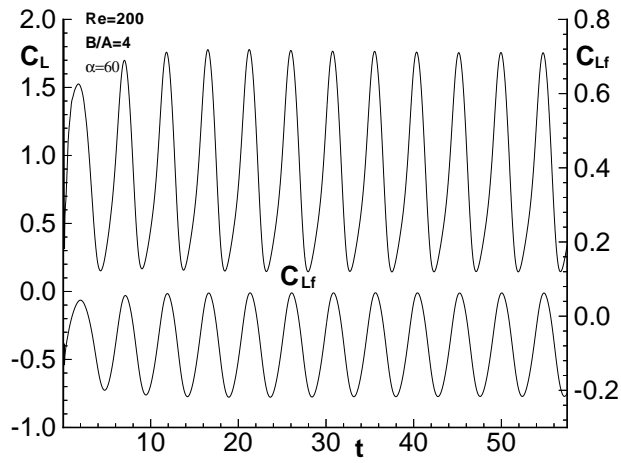
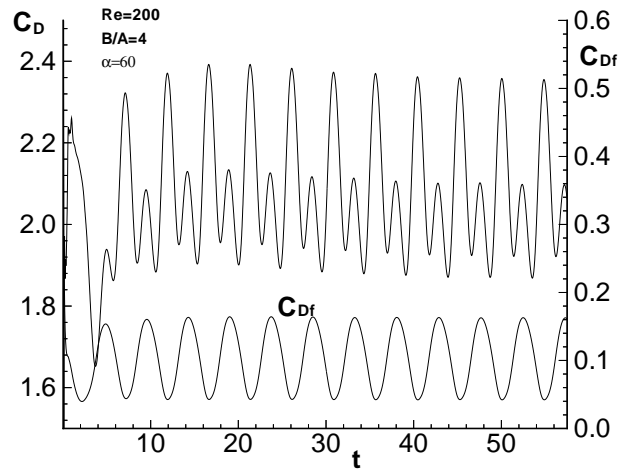


Figure 10: Time history of drag, lift and moment coefficients.

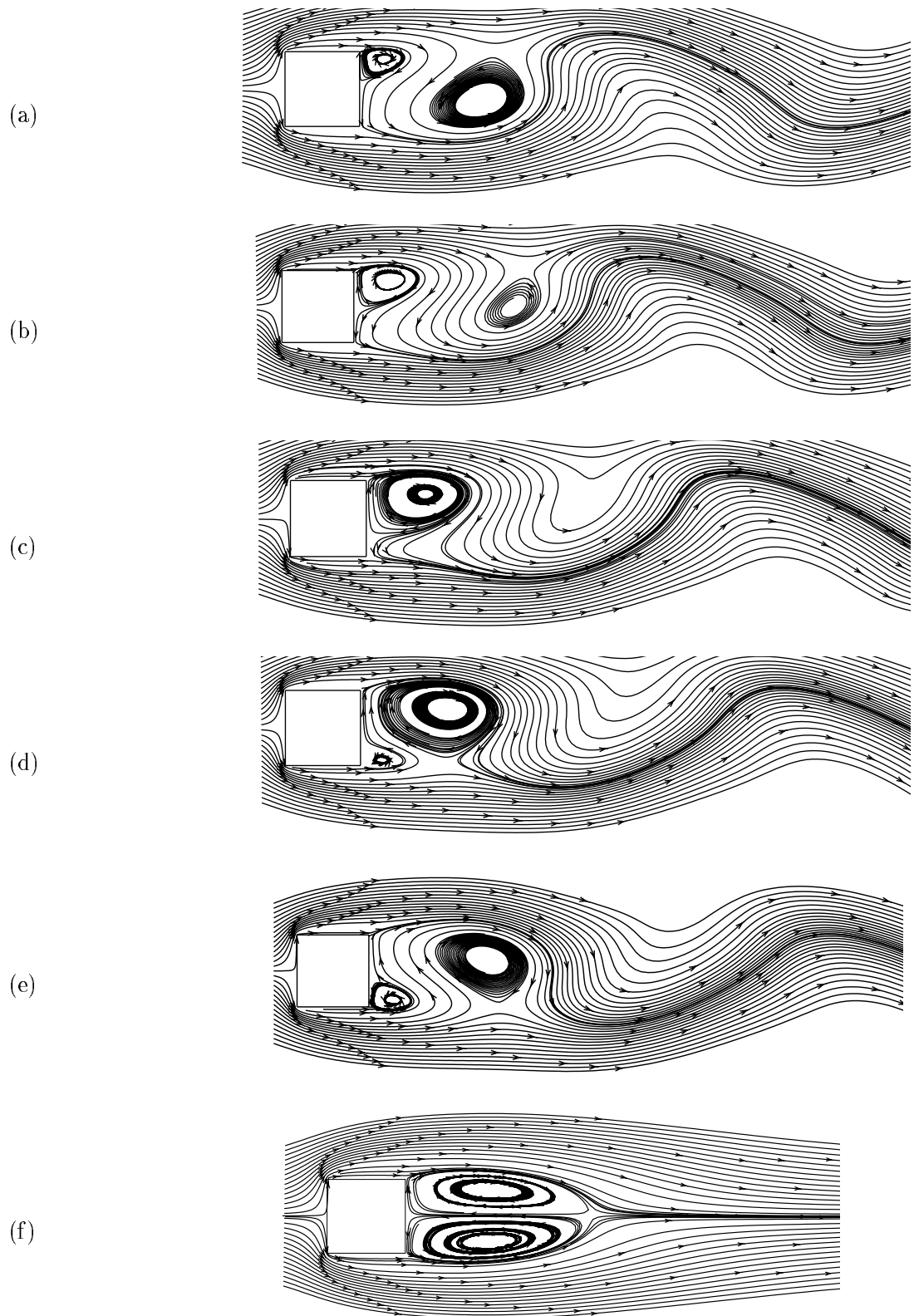


Figure 11: Time sequence, (a) - (e), see Fig. 9, of streamlines for $Re = 75$ in half period of vortex shedding, (f) Time average streamlines.

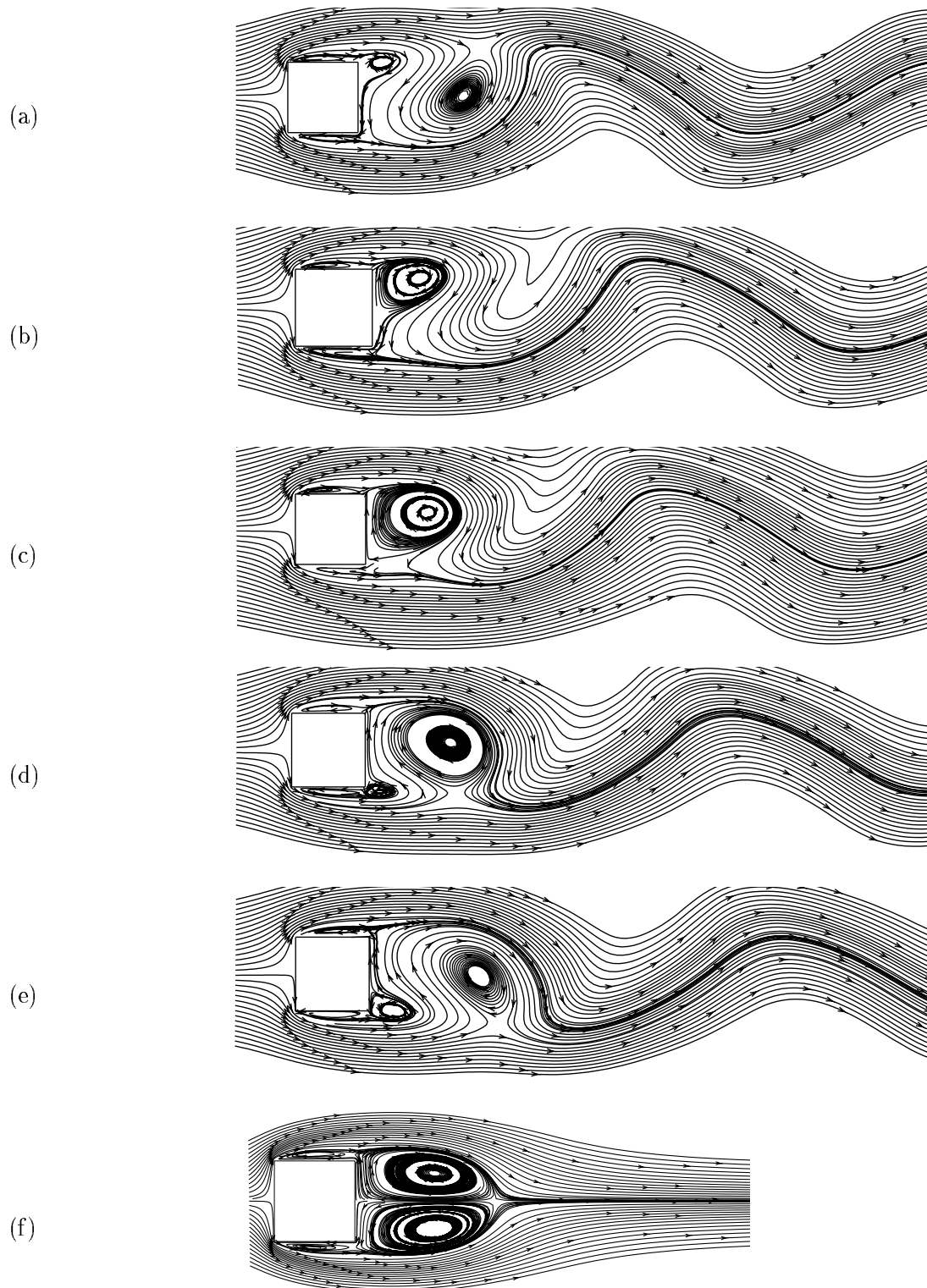


Figure 12: Time sequence, (a) - (e), see Fig. 9, of streamlines for $Re = 200$ in half period of vortex shedding, (f) Time average streamlines.

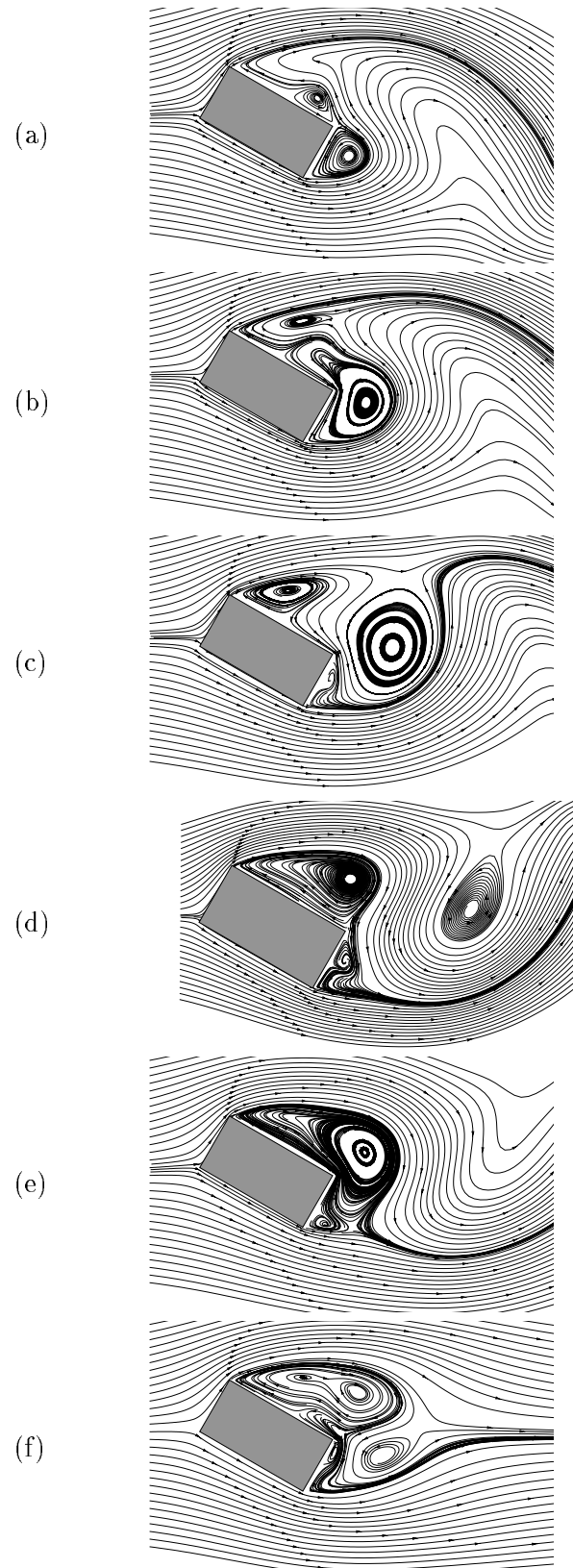


Figure 13: Time sequence, (a) – (e), see Fig. 9, of streamlines for $Re = 200$, $B/A = 2$ and $\alpha = 30^\circ$ in one period of vortex shedding, (f) Time average streamlines.

h/d	St	C_D	C_{D_p}	$C_{p,f}$	$C_{L'}$	$C_{D'}$	$-C_{pb}$	C_{ps}	L_r
0.25	.180	2.095	2.049	.670	.303	.049	1.339	1.035	1.22
0.50	.165	1.767	1.723	.696	.277	.022	.998	1.037	1.42
0.75	.153	1.562	1.519	.714	.196	.009	.782	1.035	1.83
1.00	.145	1.444	1.398	.726	.130	.0019	.623	1.048	2.22
2.00	.132	1.300	1.220	.740	.044	.0043	.463	1.042	2.75
2.50	.128	1.279	1.180	.743	.038	.0041	.419	1.042	2.77
3.00	.125	1.275	1.152	.746	.0041	.0040	.389	1.043	2.75
4.00	.121	1.286	1.116	.748	.0055	.0038	.349	1.043	2.72

Table 8: Effect of projected side ratio h/d for $Re = 100$

h/d	St	C_D	C_{D_p}	$C_{p,f}$	$C_{L'}$	$C_{D'}$	$-C_{pb}$	C_{ps}	L_r
0.25	.200	2.424	2.420	.563	.552	.1465	1.930	1.018	.79
0.50	.191	2.004	2.020	.588	.619	.0951	1.455	1.016	.81
0.75	.170	1.617	1.649	.636	.416	.0366	1.006	1.020	1.27
1.00	.165	1.424	1.464	.662	.240	.0121	.796	1.023	1.71
2.00	.169	1.183	1.234	.679	.133	.0066	.543	1.025	1.79
3.00	.158	1.082	1.125	.690	.203	.0047	.423	1.026	1.90
4.00	.146	1.015	1.049	.700	.110	.0037	.338	1.028	2.52

Table 9: Effect of projected side ratio h/d for $Re = 200$

separation points are located at the leeward corners, but at $Re = 200$, they are located at the windward corners with back flow occurring at the side surface. Up to $h/d = 1$ this back flow covers the whole surface but by increasing the side ratio the attachment points appear at the side surfaces which cause a jump in the value of the Strouhal number, as seen in Fig. 14. A compilation of various quantities at different projected side ratios and at $Re = 100, 200$ can be found in Tables 8 and 9.

9.9 Influence of Angle of Incidence

At $Re = 200$, an extensive investigation of the influence of the angle of incidence from 0° to 90° and at side ratios $B/A = 1, 2, 4$ was performed. The results for Strouhal number, drag, RMS drag, pressure drag, lift, pressure lift, RMS lift, moment, ratios of pressure drag to drag stagnation pressure coefficients and Strouhal number are presented in Figs. 15 to 20

The variation of the time-averaged drag coefficient with the angle of incidence is shown in Fig. 15. For side ratios 1 and 2, the drag coefficient has a minimum at around $\alpha = 6^\circ$ and a second minimum at around angles of incidence 84° ($B/A = 1$) and 70° ($B/A = 2$). At $B/A = 4$, however, the drag coefficient increases monotonically with increasing angle of incidence. The behavior of C_D at $B/A = 1$ is different from side ratio 2 and 4, and this is because of symmetry of the square cylinder. Because of this fact, the same trend (but in the opposite direction) occurs between $\alpha = 0^\circ - 45^\circ$ and $\alpha = 45^\circ - 90^\circ$ for all quantities (see Figs. 15 - 20). Fig. 15 shows that for $0^\circ < \alpha < 45^\circ$ an increase in side ratio gives an increase in C_D , whereas but vice versa for $\alpha > 45^\circ$.

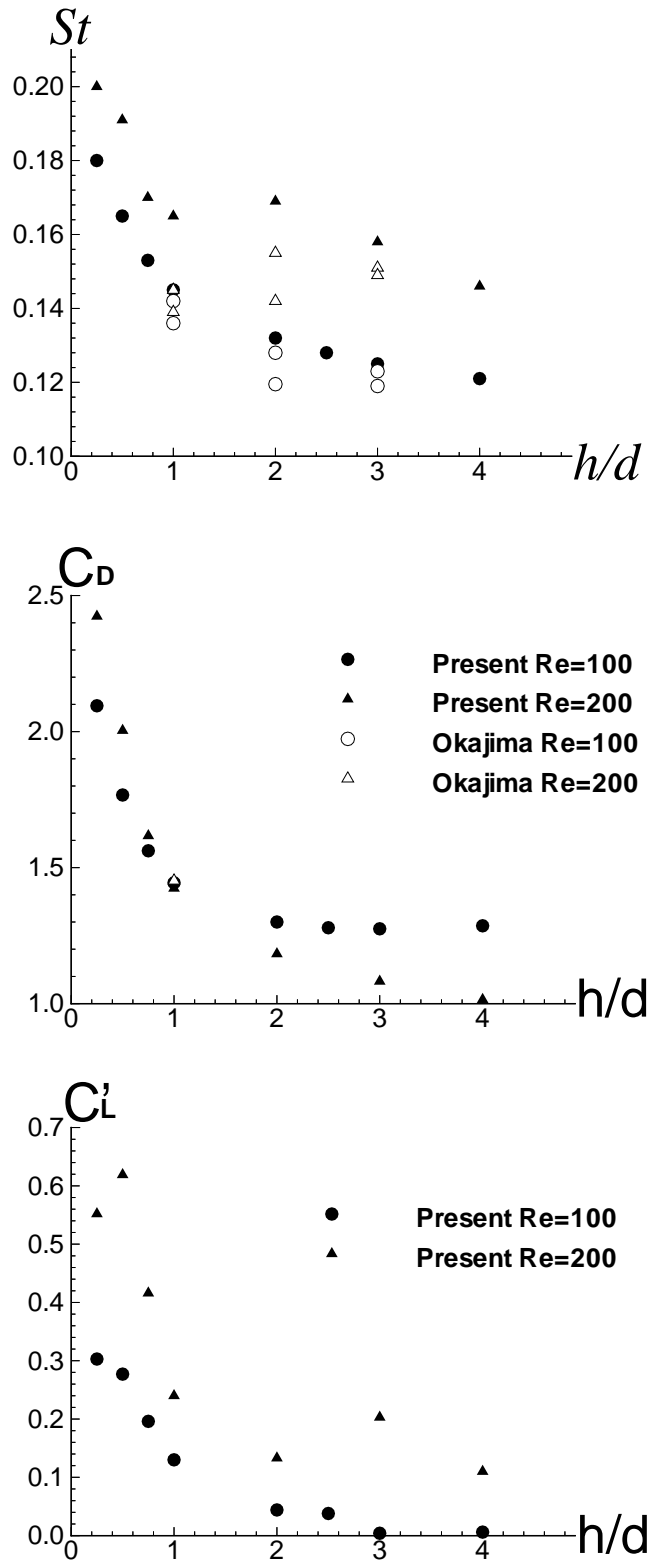


Figure 14: Strouhal number, drag and RMS lift coefficient *vs.* projected side ratio.

At low angles of incidence and high angles of incidence ($\alpha \geq 80^\circ$) the pressure drag coefficients are greater than the total drag coefficient, which means that the friction drag is negative (see Fig. 16). This is due to a large back-flow regime along the sides. Between these two ranges friction drag is positive and the maximum value is 16% of the total drag when $B/A = 4$ and $\alpha = 30^\circ$. When $B/A = 2$ and $\alpha = 30^\circ$, and $B/A = 1$ and $\alpha = 45^\circ$, the friction drag decreases to 12% and 11%, respectively.

In Figs. 17 and 18, the variation of the time-averaged lift and RMS lift coefficients with the angle of incidence are shown. As is seen in Fig. 17, C_L increases from zero to a maximum value at angles of incidence 30° and 10° , for side ratios 2 and 4, respectively, and then decreases to zero at $\alpha = 90^\circ$. Two peak values of C_L for $B/A = 1$ are seen at 6° and 84° . The values of C_L sharply increase by increasing the side ratio, for instance, the peak value for $B/A = 4$ is two times greater than for $B/A = 2$. The behavior of C_L with angle of incidence for different side ratio is approximately the same as for C_D up to $\alpha = 45^\circ$ but then it decreases with further increase in α .

The time-averaged moment coefficients acting on the body due to pressure and friction forces were calculated for different angles of incidence and side ratios and the results are depicted in Fig. 19. The moments were computed with respect to the geometrical center of the body. The variation of C_M with angle of incidence for different side ratios does not show the same trend as shown in Fig. 19. The peak values are located at $\alpha = 10^\circ, 6^\circ$ and 10° for side ratios 1, 2 and 4, respectively. For $B/A = 2$, it is seen another peak at $\alpha = 30^\circ$. The magnitude of C_M sharply increases when the side ratio is increased.

Strouhal numbers versus angles of incidence for different side ratios are shown in Fig. 20. As is seen in Fig. 20, Strouhal number does not vary smoothly at $\alpha \leq 20^\circ$. For higher angles of incidence, however, the Strouhal number increases smoothly to a maximum value and then decreases. The maximum value of Strouhal number occurs at $\alpha = 45^\circ, 60^\circ$ and 75° for $B/A = 1, 2$ and 4, respectively.

Figs. 15 - 20 show that the behavior of all quantities at low angles of incidence ($\alpha \leq 20^\circ$) and high angles of incidence ($\alpha \geq 70^\circ$) is different from that in the region between these two values. This difference is stronger at low angle of incidences than at high angles of incidence. This is probably due to the degree of reattachment and/or separation on each side of the cylinder in the wake flow and to the fact that the interactions in the near-wake region will have a strong influence on the shedding period.

It is found that the two separation points are fixed at the two corners which are located on projected side, e.g. at zero incidence these points are fixed on the upper and lower windward corners, and at an incidence of less than 45° they are fixed on the upper leeward and lower windward corners. By changing the angle of incidence the width of the wake is changed and this is one of the most important parameters which influences on the results. At low angles of incidence, especially at high side ratios, the separated flow reattaches at the side surfaces in the period of shedding, and a second set of vortices shed from the other corners in the wake flow. The above comments can explain results for both low and high angles of incidence.

Conclusions

Numerical calculations of vortex shedding past a rectangular cylinder at incidence have been reported For $Re \leq 200$, $\alpha = 0^\circ - 90^\circ$ and $B/A = 1, 2, 4$. Apart from the physical parameters investigated, i.e. Reynolds number, body side ratio, angle of incidence and blockage, it was found

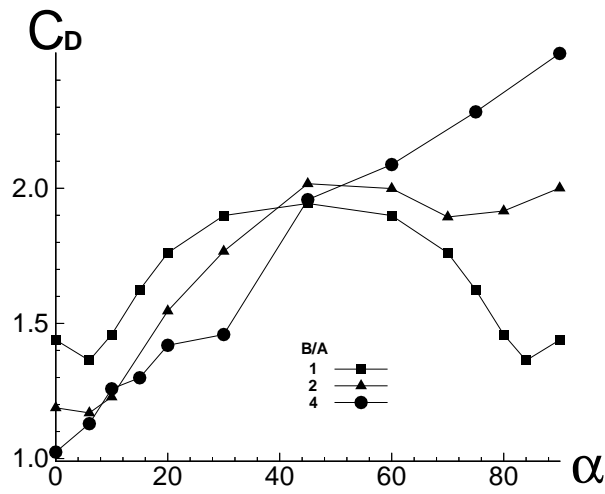


Figure 15: Drag coefficient vs angle of incidence for $Re = 200$, $X_u=10$, $X_d=25$

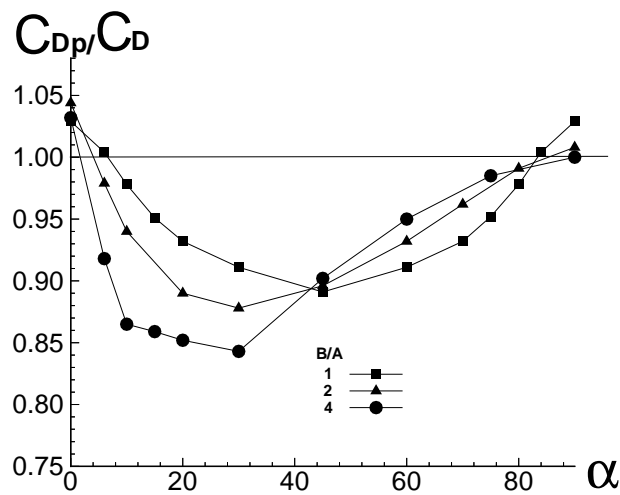


Figure 16: Ratio of pressure drag to drag coefficient *vs.* angle of incidence for $Re = 200$, $X_u=10$, $X_d=25$

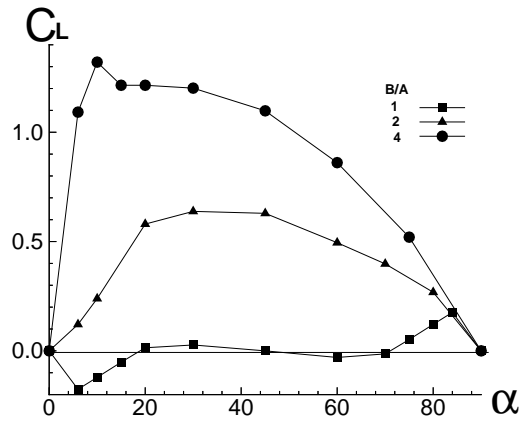


Figure 17: Lift coefficient *vs.* angle of incidence for $Re = 200$, $X_u=10$, $X_d=25$

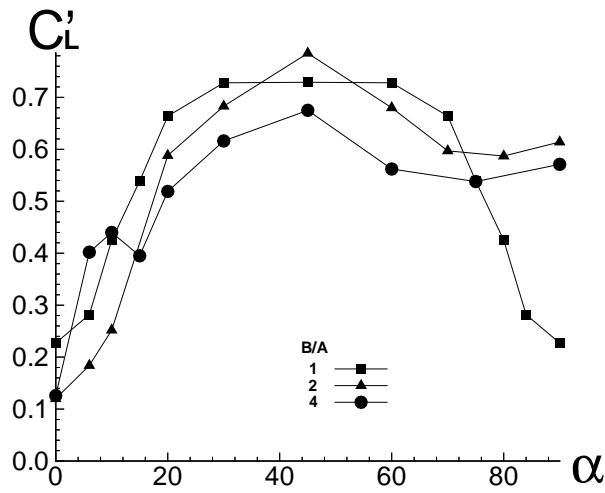


Figure 18: RMS lift *vs.* angle of incidence for $Re = 200$, $X_u=10$, $X_d=25$

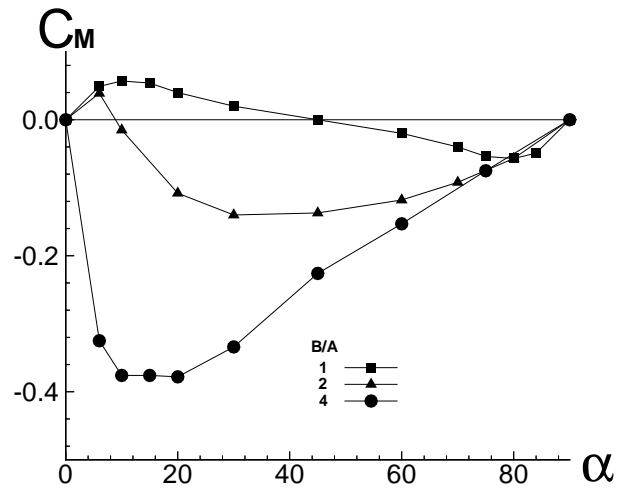


Figure 19: Moment coefficient *vs.* angle of incidence for $Re = 200$, $X_u=10$, $X_d=25$

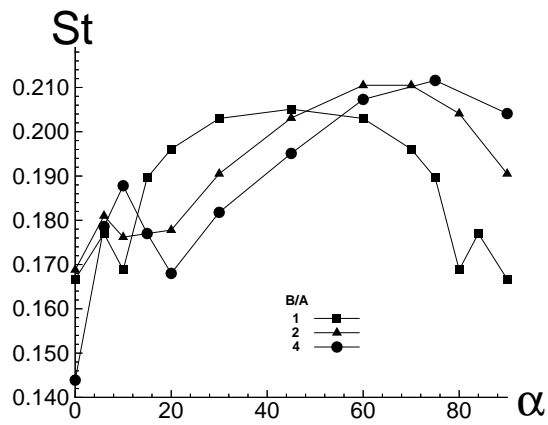


Figure 20: Strouhal number *vs.* angle of incidence for $Re = 200$, $X_u=10$, $X_d=25$

that the results also were strongly dependent on various numerical parameters such as time step, domain size and spatial resolution in both far and near field. Some of the discrepancies between present results and those from previous numerical studies have to be attributed to differences in the above mentioned numerical parameters.

By using the Strouhal number or drag coefficients as an indicator for comparison of the results, some of these effects do not show up correctly. However, when using the RMS lift coefficient as an indicator the strong sensitivity to various numerical parameters was demonstrated.

By increasing the projected side ratio there was a significant decrease in Strouhal number. For instance, at $Re = 100$, when going from $h/d = 0.25$ to $h/d = 4$, there was a smooth 33% decrease in Strouhal number. At $Re = 200$, the corresponding decrease was 27% but in this case a kink at around $h/d = 2$ was observed and this is due to attachment of flow occurring on the sides aligned with the flow.

It is concluded that the behavior of all quantities at low angles of incidence (approx. $\alpha \leq 20^\circ$) and at high angles (approx. $\alpha \geq 70^\circ$) is significantly different from that in between these regions. This is due to fundamentally different evolutions of flow features close to the cylinder.

References

- [1] M. P. Arnal, D. J. Goering, and J.A.C. Humphrey. Vortex shedding from a bluff body adjacent to a plane sliding wall. *J. Fluids Eng., Trans. ASME*, 113:384–398, 1991.
- [2] H. B. Awbi. Effect of blockage on the strouhal number of 2-d bluff bodies. *J. of Wind Eng. and Ind. Aero.*, 12:353–363, 1983.
- [3] P. W. Bearman and E. D. Obasaiu. An experimental study of pressure fluctuations on fixed and oscillating square-section cylinders. *J. Fluid Mech.*, 119:297–321, 1982.
- [4] P. W. Bearman and D. M. Trueman. An investigation of the flow around rectangular cylinders. *Aeronautical Quarterly*, 23:229–237, 1972.
- [5] S. M. Belotserkovsky, V. N. Kotovskii, M. I. Nisht, and R.M. Federov. Two-dimensional separated flows. Technical report, CRC Press, Boca Roton, Florida, 1993.
- [6] R.D. Blevins. *Flow-Induced Vibration*. Van Nostrand Reinhold, New York, 1990.
- [7] A. K. Bokaian and F. F. Geoola. On the cross flow response of cylindrical structures. In *Proc. Inst. Civil Engineering*, volume 75, pages 379–418, 1983.
- [8] A. K. Bokaian and F. Geoola. Hydrodynamics galloping of rectangular cylinders. In H. S. Stephens and G. B. Warren, editors, *Int. Conf. Flow-Induced Vibrations In Fluids Engineerings*, pages 105–129, Reading, England, 1982.
- [9] B. R. Bostock and W. A. Mair. Pressure distributions and forces on rectangular and d-shaped cylinders. *Aeronautical Quarterly*, 23:1–6, 1972.
- [10] M. Braaten and W. Shyy. A study of recirculating flow computation using body-fitted coordinates: Consistency aspects and mesh skewness. *Num. Heat Transfer*, 9:559–574, 1986.
- [11] A.D. Burns and N.S. Wilkes. A finite difference method for the computation of fluid flows in complex three-dimensional geometries. Aere R 12342, Harwell Laboratory, England, 1987.

- [12] S. S. Chen. *Flow-induced vibration of circular cylindrical structures*. Hemisphere publishing corporation, 1987.
- [13] L. Davidson and B. Farhanieh. CALC-BFC: A finite-volume code employing collocated variable arrangement and cartesian velocity components for computation of fluid flow and heat transfer in complex three-dimensional geometries. Rept. 92/4, Thermo and Fluid Dynamics, Chalmers University of Technology, Gothenburg, 1992.
- [14] R.W. Davis and E.F Moore. A numerical study of vortex shedding from rectangles. *J. Fluid Mech.*, 116:475–506, 1982.
- [15] R.W. Davis, E.F. Moore, and L.P. Purtell. A numerical-experimental study of confined flow around rectangular cylinders. *Phys. Fluids*, 27:46–59, 1984.
- [16] R. Franke, W. Rodi, and B. Schöning. Numerical calculation of laminar vortex-shedding flow past cylinders. *J. Wind Eng. Ind. Aero.*, 35:237–257, 1990.
- [17] J. E. Fromm and F. H. Harlow. Numerical solution of the problem of vortex street development. *Physics of Fluids*, 6:975–982, 1963.
- [18] I. Grant and F. H. Barnes. The vortex shedding associated with structural angles. *J. of Wind Eng. and Ind. Aero.*, 8:115–122, 1981.
- [19] O. M. Griffin. A note on bluff body vortex formation. *J. Fluid Mech.*, 258:217–224, 1995.
- [20] M.A.Z. Hasan. The near wake structure of a square cylinder. *Int. J. Heat and Fluid Flow*, 10:339–348, 1989.
- [21] C. P. Jackson. A finite-element study of the onset of vortex shedding in flow past variously shaped bodies. *J. Fluid Mech.*, 182:23–45, 1987.
- [22] T. Von Kármán. Über den Mechanismus des Widerstandes, den ein bewegter Körper in einer Flüssigkeit erzeugt. *Nachr. Ges. Wiss. Göttingen Math.-Phys. Klasse II*, pages 509–517, 1911.
- [23] K. M. Kelkar and S. V. Patankar. Numerical prediction of vortex shedding behind a square cylinder. *Int. J. Num. Methods in Fluids*, 14:327, 1992.
- [24] C.W. Knisely. Strouhal numbers of rectangular cylinders at incidence: A review and new data. *J. of Fluids and Structures*, 4:371–393, 1990.
- [25] B. E. Lee. The effect of turbulence on the surface pressure field of a square prism. *J. Fluid Mech.*, 69:263–282, 1975.
- [26] B.P. Leonard. A stable and accurate convective modeling based on quadratic upstream interpolation. *Comp. Meth. Appl. Mech. Eng.*, 19:59–98, 1979.
- [27] G. Li and A. C. Humphrey. Numerical modeling of confined flow past a cylinder of square cross-section at various orientations. *Int. J. for Numerical Methods in Fluids*, 20:1215–1236, 1995.
- [28] S.C Luo, Md.G. Yazdani, Y.T. Chew, and T.S. Lee. Effects of incidence and afterbody shape on flow past bluff cylinders. *J. Wind Eng. Ind. Aero.*, 53:375–399, 1994.
- [29] T.F. Miller and F.W. Schmidt. Use of a pressure weighted interpolation method for the solution of the incompressible navier-stokes equations on a non-staggered grid system. *Numer. Heat Transfer*, 14:213–233, 1980.

- [30] V. J. Modi and J. E. Slater. Unsteady aerodynamics and vortex induced aeroelastic instability of a structural angle section. *J. of Wind Eng. and Ind. Aero.*, 11:321–334, 1983.
- [31] P. A. Monkewitz, C. H. K. Williamson, and G. D. Miller. Phase dynamics of Kármán vortices in cylinder wakes. *Phys. Fluids*, 8:91, 1996.
- [32] S. Nagano, M. Naito, and H. Takata. A numerical analysis of two-dimensional flow past a rectangular prism by a discrete vortex model. *Computers & Fluids*, 10:243–259, 1982.
- [33] H. Nakaguchi, K. Hashimoto, and S. Muto. An experimental study on aerodynamic drag of rectangular cylinders. *J. Japan Soc. Aero. Space Sci.*, 16:1–5, 1968.
- [34] C. Norberg. Flow around rectangular cylinders: Pressure forces and wake frequencies. *J. Wind Eng. Ind. Aero.*, 49:187–196, 1993.
- [35] C. Norberg. An experimental investigation of the flow around a circular cylinder: Influence of aspect ratio. *J. Fluid Mech.*, 258:287–316, 1994.
- [36] J. Novak. Strouhal number of a quadrangular prism, angle iron, and two circular cylinders arranged in tandem. In *Acta Technical CSAV*, pages 361–373, Czechoslovakia, 1974.
- [37] M. Novak. Galloping and vortex induced oscillations of structures. In *Third Int. Conf. Wind Effects on Buildings and Structures*, pages 799–809, Tokyo, Japan, 1966.
- [38] E. D. Obasaju. An investigation of the effects of incidence on the flow around a square section cylinder. *Aeronautical Quarterly*, 34:243–259, 1983.
- [39] Y. Ohya, K. Washizu, K. Fujii, and Y. Otsuki. Wind tunnel experiments on aerodynamic forces and pressure distributions of rectangular cylinder in a uniform flow. *J. Fluids Structures.*, 1980.
- [40] A. Okajima. Strouhal numbers of rectangular cylinders. *J. Fluid Mech.*, 123:379–398, 1982.
- [41] A. Okajima. Numerical simulation of flow around rectangular cylinder. *J. Wind Eng. Ind. Aero.*, 33:171–180, 1990.
- [42] A. Okajima. Numerical analysis of the flow around an oscillating cylinder. In *6th Int. Conf. Flow-Induced Vibration*, London, U.K., 1995.
- [43] A. Okajima, T. Nagahisa, and A. Rokugoh. A numerical analysis of flow around rectangular cylinders. *JSME Int. J. Ser. II*, 33:702–711, 1990.
- [44] A. Okajima, H. Ueno, and H. Sakai. Numerical simulation of laminar and turbulent flows around rectangular cylinders. *Int. J. for Numerical Methods in Fluids*, 15:999–1012, 1992.
- [45] Y. Otsuki, K. Fujii, K. Washizu, and A. Ohya. Wind tunnel experiments on aerodynamics forces and pressure distributions of rectangular in a uniform cylinders in a uniform flow. In *Proceeding of the Japan Symposium on Wind-Structure Interaction*, pages 169–176, 1978.
- [46] Y. Otsuki, K. Washizu, H. Tomizawa, and A. Ohya. A note on the aeroelastic instability of a prismatic bar square section. *J. of Sound and Vibration*, pages 233–248, 1974.
- [47] R. Parker and M. C. Welsh. Effects of sound on flow separation from blunt flat plates. *Int. J. Heat and Fluid Flow*, 4:113–127, 1983.
- [48] G. Parkinson. Phenomena and modeling of flow-induced vibrations of bluff bodies. *Prog. Aerospace Sci.*, 26:169–224, 1989.

- [49] G.V. Parkinson. Wind-induced instability of structures. *Phil. Trans. Roy. Soc. London A*, 269:395–409, 1971.
- [50] S.V. Patankar. *Numerical Heat Transfer and Fluid Flow*. McGraw-Hill, New York, 1980.
- [51] M. Peric, Kessler, and G. Scheuerer. Comparison of finite-volume numerical methods with staggered and collocated grids. *Computers & Fluids*, 16:389–403, 1988.
- [52] M. Provansal, C. Mathis, and L. Boyer. Bénard-von Kármán instability: transient and forced regimes. *J. Fluid Mech.*, 182:1–22, 1987.
- [53] C.M. Rhie and W.L. Chow. Numerical study of the turbulent flow past an airfoil with trailing edge separation. *AIAA J.*, 21:1527–1532, 1984.
- [54] D. O. Rockwell. Organized fluctuations due to flow past a square cross section cylinder. *ASME J. of Fluids Engineering*, 99:511–516, 1977.
- [55] W. Rodi. On the simulation of turbulent flow past bluff bodies. *J. Wind Eng. Ind. Aero*, 46:3–19, 1993.
- [56] J. Y. Sa and K. S. Chang. Shedding patterns of the near-wake vortices behind a circular cylinder. *J. Num. Methods Fluids*, 12:463–474, 1991.
- [57] M. Schumm, E. Berger, and P. A. Monkewitz. Self-excited oscillations in the wake of two-dimensional bluff bodies and their control. *J. Fluid Mech.*, 253:17–35, 1994.
- [58] W. Shyy, S.S Tong, and S.M. Correa. Numerical recirculating flow calculation using body-fitted coordinate system. *Num. Heat Transfer*, 8:99–113, 1985.
- [59] Sohankar, L. Davidson, and C. Norberg. Numerical simulation of unsteady flow around a square two-dimensional cylinder. In *12th Australasian Fluid Mechanics Conference*, pages 517–520, The University of Sydney, Australia, 1995.
- [60] V. Strouhal. Über eine besondere Art der Tonerregung. *Ann. Physik und Chemie, Neue Folge*, 5:216–251, 1878.
- [61] T. Tamura, E. Krause, S. Shirayama K. Ishii, and K. Kuwahara. Three-dimensional computation of unsteady flows around a square cylinder. In *11th International Conference on Numerical Methods in Fluid Dynamics*, Williamsburg, 1988.
- [62] T. Tamura and K. Kuwahara. Numerical study of aerodynamics behavior of a square cylinder. *J. of Wind Eng. and Ind. Aero.*, 33:161–170, 1990.
- [63] T. Tamura, I. Ohta, and K. Kuwahara. On the reliability of two-dimensional simulation for unsteady flows around a cylinder-type structure. *J. of Wind Eng. and Ind. Aero.*, 35:275–288, 1990.
- [64] J. F. Thompson, Z.U.A. Warsi, and C. W. Mastin. *Numerical Grid Generation; Foundations and Applications*. Elsevier Science, 1985.
- [65] B. van leer. Towards the ultimate conservative difference scheme. Monotonicity and conservation combined in a second order scheme. *Journal of Computational Physics*, 14:361–370, 1974.
- [66] B. van leer. Towards the ultimate conservative difference scheme. V. A second-order sequel to godonov’s method. *Journal of Computational Physics*, 32:101–136, 1979.

- [67] B. J. Vickery. Fluctuating lift and drag on a long cylinder of square cross-section in a smooth and in a turbulent stream. *J. Fluid Mech.*, 25:481–494, 1966.
- [68] K. Washizu, A. Ohya, Y. Otsuki, and K. Fujii. Aeroelastic instability of rectangular cylinders in a heaving mode. *J. Sound and Vibration*, 59:481–494, 1978.
- [69] C. H. K. Williamson. Vortex dynamics in the cylinder wake. *Ann. Rev. Fluid Mech.*, 28:477–539, 1996.
- [70] T. G. Zaki, M. Sen, and M Gad-El-Hak. Numerical and experimental investigation of flow past a freely rotationable square cylinder. *J. Fluids and Structures*, 8:555, 1994.

Nomenclature

A	The shortest side of the cylinder
B	The longest side of the cylinder
C_D	Total drag coefficient
$C_{D'}$	RMS drag coefficient
C_{D_p}	Pressure drag coefficient
C_{D_f}	friction drag coefficient
C_L	Total lift coefficient
C_{L_p}	Pressure lift coefficient
C_{L_f}	friction lift coefficient
$C_{L'}$	RMS lift coefficient
C_M	Total moment coefficient
C_{pb}	Base pressure coefficient at centerline
C_{ps}	Stagnation pressure coefficient
$C_{p,f}$	Surface averaged frontal side C_p
$C_{p,tb}$	Surface averaged top and bottom side C_p
d	Projected width in the streamwise direction ($= A \cos \alpha + B \sin \alpha$)
f_S	Shedding frequency
h	Projected length in the cross-stream direction ($= A \sin \alpha + B \cos \alpha$)
H	Height of computational domain
L_r	Time mean length of recirculating region
Re	Reynolds number, $U_\infty d / \nu$
St	Strouhal number, $f_S d / U_\infty$
t	Non-dimensional time (scaled with d / U_∞)
U	Streamwise velocity
U_∞	Free stream velocity
V	Cross stream velocity
X_d	Extent of domain downstream of body
X_u	Extent of domain upstream of body
α	Angle of incidence
β	Blockage ($= d / H$)
δ	Minimum cell size adjacent to the body
Δ	Maximum cell size in far field
Δt	Non-dimensional time step
ν	Kinematic viscosity
ρ	Fluid density